Physics – Uspekhi **66** (7) 647 – 672 (2023)

REVIEWS OF TOPICAL PROBLEMS

PACS numbers: **71.30.+h**, 75.30.Cr, 75.30.Et, 75.47.Lx, 75.50.Pp

Features of spin crossovers in magnetic materials

Yu S Orlov, S V Nikolaev, V A Dudnikov, V A Gavrichkov, S G Ovchinnikov

DOI: https://doi.org/10.3367/UFNe.2022.05.039195

Contents

Abstract. **We present experimental and theoretical results of spin crossover studies in magnetically ordered materials. The effect of spin crossovers on the electronic structure of transition metal oxides and on the Bose condensation of spin excitons in the vicinity of the spin crossover is considered. A new method for calculating the interatomic superexchange interaction in transition metal oxides is discussed that allows considering selective contributions of excited magnetic cation terms. Changes in the exchange interaction sign are predicted for spin crossovers for d^5-d^7 ions. In the $RCoO_3$ family of rare-earth cobaltites, the ground state is nonmagnetic, but, as the temperature increases, thermal excitations of high-spin states give rise to a number of experimentally detectable features. In defective $RCoO_3$ samples, stabilization of the high-spin term and ferromagnetic ordering are possible. Dynamical crossovers under external pumping and the dynamics of multiplicity, magnetization, and local lattice distortions are discussed. Geophysical implications of spin crossovers are considered, and metallic properties of Earth's mantle at a depth of 1400–1800 km are predicted.**

Keywords: spin crossovers, exchange interaction, Bose condensation, spin excitons, transition metal oxides, rare earth cobaltites, strong electron correlations, antiferromagnetism, ferromagnetism, metal–insulator transition, Earth's mantle, Hubbard model

Yu S Orlov [1,2,a], **S V Nikolaev** [1,2,b], **V A Dudnikov** [1,c], **V A Gavrichkov** [1,d], **S G Ovchinnikov** [1,2,e]
[1] Kirensky Institute of Physics,
Federal Research Center Krasnoyarsk Science Center,
Siberian Branch of the Russian Academy of Sciences,
Academgorodok 50, str. 38, 660036 Krasnoyarsk, Russian Federation
[2] Siberian Federal University,
prosp. Svobodny 79, 660041 Krasnoyarsk, Russian Federation
E-mail: [a]orlov@iph.krasn.ru, [b]25sergeyn@mail.ru,
[c]slad63@yandex.ru, [d]gav@iph.krasn.ru, [e]sgo@iph.krasn.ru

Received 17 November 2021, revised 12 April 2022
Uspekhi Fizicheskikh Nauk **193** (7) 689 – 716 (2023)
Translated by S Alekseev

1. Introduction

Spin crossover (SCO) is the phenomenon of a spin state change in some 3d metal compounds. The terms 'spin transition' and 'spin equilibrium' are also sometimes used in the literature. Historically, the first SCOs were discovered in organometallic complexes, for example, in Fe-tris (dimethyldithiocarbamate) [1], discerned from anomalies in the temperature dependence of the magnetic susceptibility. SCOs are usually found in complexes of 3d metals with d^4-d^7 ionic configurations with an octahedral symmetry of ligands under changes in external factors, most often the temperature or pressure [2, 3]. The change in the spin state during SCO is typically related to a change in the ground state between the high-spin (HS) and low-spin (LS) configurations [4]. In organometallic complexes, SCO sometimes also occurs under irradiation by light [3], so-called light-induced excited spin-state trapping (LIESST).

In inorganic crystals of 3d metal oxides, SCO is typically observed at high (most often, megabar) pressures (see review

[5]). Switching between the LS and HS states of Co^{3+} with increasing temperature is observed in $LaCoO_3$ and other rare-earth cobaltites (see review [6]). The SCO in oxide crystals has two features setting it apart from the SCO in organometallic complexes. In the latter, metal–ligand complexes are usually arranged irregularly and are located far from each other, and the SCO mechanism is therefore mainly determined by the effect of the ligand field on the electron states of the cation. In fact, the single-ion approach is applicable to the description of the many-electron states of a cation in the crystal field of ligands [7–9]. Within this approach, the SCO, without taking the interaction with the lattice into account, is not a thermodynamic phase transition, but at zero temperature it becomes a quantum phase transition with a geometric order parameter [10]. In oxides, cations are located at close-packed lattice sites surrounded by oxygen octahedra, and the super-exchange interaction of neighboring cations leads to cooperative effects that turn the SCO into a first-order thermodynamic phase transition [11]. Interaction with the lattice also leads to cooperative effects in both organometallic complexes and crystals. In organometallic complexes, cooperative effects, usually modeled in terms of the effective Ising model, can also lead to first-order phase transitions [12–15].

The physics of SCO is at the intersection of many branches of condensed matter physics: electronic properties of strongly correlated systems, magnetism, superconductivity, and phase transitions. Due to the significant (about 10%) difference between the ionic radii of the LS and HS states, SCO is accompanied by strong structural anomalies and significant anharmonicity. As the electron states change, the optical properties of the crystal also change. Thus, SCO studies are of general physical interest. There are also geophysical consequences of SCOs deep in Earth's lower mantle, which are also discussed in this review. In magnetic materials, SCO acquires additional features, which are considered in Sections 4 and 5.

In addition, there is also applied interest in materials exhibiting SCO for applications in electronic and optoelectronic devices [16]. The SCO phenomenon can in principle be used in fabricating switches, data storage devices, and optical displays. Possible applications of SCO can use the HS–LS bistability, giving rise to color and magnetism changes in samples [3]. Molecular switches, like electrical switches, require an on/off mechanism, which is achieved by sudden spin transitions with hysteresis. To reduce the size of data storage devices while increasing their capacity, smaller structural units (such as molecules or cation–anion octahedra) are required that exhibit bistability and thermal hysteresis [3]. The research goals include developing new materials in which the SCO response time can be reduced from a few nanoseconds to a few femtoseconds.

2. Main experimental methods for studying spin crossovers

We do not intend to give a detailed description of the experimental methods for studying SCOs for two reasons. First, they are mostly standard and well-known methods in physics. Second, review [5] contains a very detailed analysis of experimental data on various transition-metal oxides at high pressures. Among the new methods that appeared after the publication of [5], we mention studies of SCO dynamics using free electron lasers (the X-ray Free Electron Laser, XFEL).

Because of the changes in magnetic properties under SCO, magnetic susceptibility measurements are key to characterizing SCO materials. In iron compounds, Mössbauer spectroscopy is also widely used, being combined quite well with high-pressure measurements in diamond anvils.

Due to the large difference in ionic radii, SCO induces pronounced changes in structural properties. X-ray crystallography methods allow following changes in the cation–anion distance under the SCO both with temperature changes in organometallic complexes and with changes in pressure in transition-metal oxides. These changes are also clearly visible in the Raman spectra and in infrared spectroscopy.

Optical absorption spectra in the visible and infrared ranges (0.05–25 μm) were used to study electron d–d transitions from the HS state to various excited terms and the behavior of the optical absorption edge during pressure-induced SCO. High-pressure Raman spectra reveal that, along with magnetic and structural transitions, electron transitions are observed in the critical pressure region, manifesting themselves in a jump-like decrease in the optical absorption threshold energy. Examples of such effects for a number of oxide crystals are given in [5].

We also note that various synchrotron methods of X-ray spectroscopy are sensitive to the change in the spin state of terms under the SCO. These methods include X-ray emission spectroscopy (XES), which amounts to detecting Fe^{3+} HS terms in the nonmagnetic phase by the appearance of a low-energy satellite in X-ray emission spectra [17, 18]; the X-ray magnetic circular dichroism (XMCD) method, used to study the SCO in magnetite in the pressure range of 12–16 GPa [19]; synchrotron Mössbauer source (SMS) spectra and Mössbauer time spectra of nuclear forward scattering (NFS) [20, 21]; and methods of resonant inelastic X-ray scattering (RIXS), used to study changes in the spectra of electron excitations during SCO in $FeBO_3$ [22].

In recent years, it has become possible to study the dynamics of SCO, which is of great interest from the standpoint of creating new photoswitchable materials. The HS–LS transition under irradiation with light, named the LIESST effect, has been discovered [3, 23]. For example, the LIESST effect in Fe(phen)2(NCS)2 was studied using time-resolved X-ray absorption near edge spectroscopy (XANES) and optical spectroscopy on an X-ray pump–probe setup in a linear coherent light source (X-ray pump–probe at Linac coherent light source X-ray free electron laser, XPP LCLS XFEL) at Stanford [24, 25]. Light-induced LS–HS switching and subsequent relaxation revealed local deformation and vibronic oscillations of the ligands.

3. General concepts on the electron structure of 3d metal oxides with strong electron correlations

At present, various versions of the density functional theory (DFT) have achieved tremendous success not only in describing the properties of known materials but also in predicting new materials. A striking example of the success of the DFT is the prediction of high-temperature superconductivity (HTSC) in H_3S at ultrahigh pressure [26], which was later confirmed experimentally [27, 28]. However, the subject of this review, 3d metal oxides, is an example of materials with strong electron correlations, to which standard DFT methods are inapplicable. For example, for La_2CuO_4, band calculations give not an insulator but a metal with a

half-filled band at the Fermi level. This shows why properly taking strong electron correlations into account in electron structure calculations has long been an important problem in condensed matter physics. The Hubbard model, being the simplest one, has long served as a testing ground for the proposed methods (see reviews [29–31]). The LDA + U (local density approximation + U) hybrid method, with the Coulomb gap imitated by a spin-polarized gap, is widely used in calculations of the electronic structure of strongly correlated materials but is valid only at zero temperature in the magnetically ordered phase. More advanced is another well-known hybrid method, LDA + DMFT, reliant on the dynamic mean-field theory (DMFT) [32, 33], which is currently the de facto standard in the study of many-electron effects in strongly correlated systems [34–36]. The LDA + DMFT method allows obtaining solutions that interpolate between opposite limits of weak and strong correlations. At the same time, the DMFT approach does not include the dependence of the mass operator on the wave vector, which is important in the case of strong short-range order (for example, in HTSC cuprates and other quasi-two-dimensional oxides) [37]. The DMFT approximation is exact in a space of an infinitely large dimension [31]. Various methods for taking nonlocal correlations into account beyond the one-site DMFT approximation were considered in recent review [38]. One of the advantages of the DMFT method is the ability to obtain solutions that interpolate between opposite limits of weak and strong correlations. In this review, we are interested in 3d metal oxides in the Mott–Hubbard insulator states, which must be described in the regime of strong correlations. For these oxides, a less resource-intensive approach based on the experience of describing the Hubbard model and its generalizations in perturbative terms can be used [30, 39]. Applied to a realistic multiband p–d model, this approach has led to the formulation of the many-electron generalized tight-binding (GTB) method [40, 41], whose hybrid version with the parameters of the Hamiltonian of a multiband p–d model calculated in the DFT (LDA + GTB) framework was proposed in [42, 43]. Because the LDA + GTB method is less known than LDA + DMFT, for the convenience of the reader, we recall some relevant background on it in Section 3.2.

3.1 Multiband p–d model in the regime of strong correlations

The common structural element of transition-metal oxides is given by the $Me\mathrm{O}_6$ octahedra (or $Me\mathrm{O}_4$ tetrahedra). Therefore, the simplest model should include the d electrons of the cation and the p electrons of the anion, together with the various interactions between them. Such a model is called the p–d model. The simplest three-band model was proposed to describe HTSC cuprates [44, 45]. In the general case, the multiband p–d model includes all five orbitals of the d electrons of the cation and p electrons of the anion; precisely this model was used in calculating the electronic properties of $LaCoO_3$ [46] with the LDA + GTB method. The Hamiltonian of the multiband p–d model is as follows:

$$H = H_\mathrm{d} + H_\mathrm{p} + H_\mathrm{pd} + H_\mathrm{pp}\,, \tag{1}$$

$$H_\mathrm{d} = \sum_r H_\mathrm{d}(r)\,,$$

$$H_\mathrm{d}(r) = \sum_{\lambda\sigma}\left[(\varepsilon_{\mathrm{d}\lambda}-\mu)\,n^\sigma_{r\lambda} + \frac{U_\mathrm{d}}{2}\,n^\sigma_{r\lambda}\,n^{-\sigma}_{r\lambda}\right] + \sum_{\sigma\sigma'}\left(V_\mathrm{d}\,n^\sigma_{r1}\,n^{\sigma'}_{r2} - J_\mathrm{d}\,d^\dagger_{r1\sigma}\,d_{r1\sigma'}\,d^\dagger_{r2\sigma'}\,d_{r2\sigma}\right),$$

$$H_\mathrm{p} = \sum_i H_\mathrm{p}(i)\,,$$

$$H_\mathrm{p}(i) = \sum_{\alpha\sigma}\left[(\varepsilon_{\mathrm{p}\alpha}-\mu)\,n^\sigma_{i\alpha} + \frac{U_\mathrm{p}}{2}\,n^\sigma_{i\alpha}\,n^{-\sigma}_{i\alpha}\right] + \sum_{\sigma\sigma'}\left(V_\mathrm{p}\,n^\sigma_{i1}\,n^{\sigma'}_{i2} - J_\mathrm{p}\,p^\dagger_{i1\sigma}\,p_{i1\sigma'}\,p^\dagger_{i2\sigma'}\,p_{i2\sigma}\right),$$

$$H_\mathrm{pd} = \sum_{\langle i,r\rangle} H_\mathrm{pd}(i,r)\,,$$

$$H_\mathrm{pd}(i,r) = \sum_{\alpha\lambda\sigma\sigma'}\left(t_{\lambda\alpha}\,p^\dagger_{i\alpha\sigma}\,d_{r\lambda\sigma} + \mathrm{h.c.} + V_{\lambda\alpha}\,n^\sigma_{r\lambda}\,n^{\sigma'}_{i\alpha} - J_{\alpha\lambda}\,d^\dagger_{r\lambda\sigma}\,d_{r\lambda\sigma'}\,p^\dagger_{i\alpha\sigma'}\,p_{i\alpha\sigma}\right),$$

$$H_\mathrm{pp} = \sum_{\langle i,j\rangle}\sum_{\alpha\beta\sigma}\left(t_{\alpha\beta}\,p^\dagger_{i\alpha\sigma}\,p_{j\beta\sigma} + \mathrm{h.c.}\right).$$

Here, H_d and H_p contain the local energies of d and p electrons with intraatomic Coulomb interactions in the same orbital (U_d and U_p) and in different orbitals (V_d and V_p), and the Hund exchange parameters J_d and J_p; i, j, and r are lattice sites, $t_{\lambda\alpha}$ is the hopping integral between 3d and 2p orbitals, α, β are p-orbital indices, and λ is the d-orbital index. The term H_pd describes the cation-anion hopping t_pd, the interatomic Coulomb interaction V_pd, and the exchange J_pd. The last term describes electron hopping between neighboring anions. The usual, although optional, assumption that the Coulomb matrix elements are independent of the orbital indices significantly reduces the number of model parameters. All model parameters are assumed to be known either from first-principle calculations or from experimental data.

For the three-band p–d model used for HTSC cuprates, the model parameters were calculated in DFT terms in [47, 48]. An important new parameter appearing in the p–d model is the charge transfer energy $E_\mathrm{CT} = \varepsilon_\mathrm{p} - \varepsilon_\mathrm{d}$. Strong electron correlations typically determine the insulating ground state of 3d metal oxides. If the minimum gap is determined by U_d (i.e., d–d excitations), then such an insulator is called a Mott–Hubbard insulator according to the Zaanen–Zavadsky–Allen classification [49]. Another limit case, where the gap is determined by E_CT (d–p excitations), corresponds to a charge-transfer insulator. However, an intermediate situation is often realized where both types of excitations are significant for the insulator gap. In particular, in perovskites, the 2p states of oxygen and the 3d states of the transition element transform under the same irreducible representations and therefore mix well. An intermediate situation is therefore realized in them, with both types of excitations being essential for determining the insulator gap.

3.2 Generalized tight-binding method for Hubbard fermions

The GTB method rests on the ideas proposed by Hubbard for describing strongly correlated electrons in the Hubbard model, developed to include a more general case of a

multiband p–d model. In the Hubbard model in the regime of strong correlations $U \gg W$ (where $W = zt$ is the band half-width, z is the number of nearest neighbors, and t is the interatomic electron hopping parameter), the free-electron band splits into two bands of Hubbard fermions: the lower (LHB) and upper (UHB). These bands play the roles of the valence and conduction bands in an ordinary insulator, but they are not described by any one-electron wave functions or operators. The term 'Hubbard fermion' refers to a Fermi-type quasiparticle whose creation changes the charge by one, as in the case of free electrons. But the commutation relations for the Hubbard fermion creation operators are complex and differ from the one-electron relations.

To clarify the concept of an electron in strongly correlated systems, to which the usual one-electron theory is inapplicable, we begin with the exact Lehmann representation for the one-electron Green's function at zero temperature [50]:

$$G_\sigma(k,\omega) = \sum_m \left(\frac{A_m(k,\omega)}{\omega - \Omega_m^+} + \frac{B_m(k,\omega)}{\omega - \Omega_m^-} \right). \tag{2}$$

The poles of this function are determined by single-particle excitations (quasiparticles) with the energies

$$\begin{aligned} \Omega_m^+ &= E_m(N+1) - E_0(N) - \mu\,, \\ \Omega_m^- &= E_0(N) - E_m(N-1) - \mu \end{aligned} \tag{3}$$

and spectral weights

$$\begin{aligned} A_m(k,\omega) &= |\langle 0, N|a_{k\sigma}|m, N+1\rangle|^2\,, \\ B_m(k,\omega) &= |\langle m, N-1|a_{k\sigma}|0, N\rangle|^2\,. \end{aligned} \tag{4}$$

Here, $|m, N\rangle$ is the mth eigenstate of the N-electron system,

$$H|m, N\rangle = E_m|m, N\rangle\,.$$

At nonzero temperatures, the Lehmann representation takes the form

$$G_\sigma^R(k,\omega) = \sum_{pq} W_q \frac{A_{pq}(k,\omega)}{\omega - \Omega_{pq}^+ + \mathrm{i}0} \left[1 + \exp\left(-\frac{\Omega_{pq}^+}{T} \right) \right].$$

A quasiparticle is now defined as an excitation from the initial state q to the final state p with the energy

$$\Omega_{pq}^+ = E_p(N+1) - E_q(N) - \mu\,. \tag{5}$$

The statistical weight of the state $|q\rangle$ is found from the Gibbs distribution with the thermodynamic potential Ω:

$$W_q = \exp\left(\frac{\Omega - E_q + \mu N}{T} \right).$$

At a nonzero temperature, both the ground and excited states, $|0, N\rangle$ and $|q, N\rangle$, are partially occupied. The quasiparticle is therefore labeled with a pair of indices (p, q). This is a one-electron excitation in a multi-electron system, occurring due to the addition of one electron to the initial N-electron state $|q, N\rangle$ with the formation of a final $(N+1)$-electron state $|p, N+1\rangle$. The energy of adding an electron is Ω_{pq}^+ in Eqn (5) and the energy of removing an electron is

$$\Omega_{pq}^- = E_p(N) - E_q(N-1) - \mu\,. \tag{6}$$

The Lehmann representation is useless in practical calculations, because the exact many-electron eigenstates $|m, N\rangle$ for a crystal are not known. The GTB method is a realization of the many-electron ideas of the Lehmann representation in the framework of the cluster perturbation theory [51]. In the GTB approach, the lattice is divided into the sum of individual clusters ($Me\mathrm{O}_6$ octahedra), the total Hamiltonian is represented as the sum of all intracluster terms H_f, $H_0 = \sum H_f$, and the sum of all intercluster terms H_{fg}, $H_{\mathrm{int}} = \sum H_{fg}$. The intracluster term H_f includes all d electrons and the nearest oxygen p-orbitals, which are orthogonalized to form molecular orbitals centered on a lattice site f (see details in [52, 53]), and all local interactions of p and d electrons. Exact numerical diagonalization of the local part provides exact multielectron eigenenergies and cluster eigenstates $H_f|p\rangle = E_p|p\rangle$. As in the usual Hubbard model, we introduce the Hubbard operators $X_f^{p,q} = |p\rangle\langle q|$, defined by a set of exact intracluster eigenstates. Then, the local part of the full Hamiltonian diagonalizes, $H_f = \sum_p E_p X_f^{p,p}$, and describes the energy of many-electron terms $|p\rangle$ in various configurations. In studying the electron structure in a system with the ground configuration d^n (where d^n is simply the notation for the hybridized term $d^n + d^{n+1}\underline{L} + d^{n+2}\underline{L}^2$, where $\underline{L}$ is a hole on the ligand, as in cluster approaches [54, 55]), three adjacent sectors of the Hilbert spaces must be considered (Fig. 1): those with n electrons (electrically neutral states), with one electron removed (the hole sector with $n-1$ electrons), and with one electron added (the electron sector with $n+1$ electrons). As a result, the intracluster exact Green's function has form (2) with the spectral weights at $T = 0$ given by $F^{p,q} = \langle X^{p,p}\rangle + \langle X^{q,q}\rangle$, which are nonzero only if at least one relevant many-electron term is occupied.

The next step in the GTB method is to include the effects of intercluster hopping and interactions, treated perturbatively. Each Fermi quasiparticle (Hubbard fermion) is defined by a pair of initial and final state indices (p, q), which are called the root vector in the diagram technique for Hubbard operators [57]. Because there are countably many such vectors, they can be enumerated and each can be assigned its own number, $m \leftrightarrow (p, q)$. One-electron annihilation/creation operators can be written as linear combinations of the Hubbard fermions, with the number m playing the role of the band index of the Hubbard fermion [58],

$$\begin{aligned} a_{f\lambda\sigma} &= \sum_m \gamma_{\lambda\sigma}(m)\, X_f^m\,, \\ a_{f\lambda\sigma}^\dagger &= \sum_m \gamma_{\lambda\sigma}^*(m)\, X_f^{\dagger m}\,, \end{aligned} \tag{7}$$

where the matrix elements, just as in formulas (4), determine the spectral weight of the quasiparticles. For the Fourier transforms of matrix Green's functions for Hubbard fermions

$$D^{m,n}(f,g) \equiv \left\langle\left\langle X_f^m \middle| X_g^{\dagger n}\right\rangle\right\rangle_E,$$

the analysis of the diagram series in the framework of the diagram technique for Hubbard operators [57] leads to exact generalized Dyson's equation [58] for spin-1/2 Fermi quasiparticles with the electric charge e:

$$\hat{D}(k,\omega) = \left[\hat{G}_0^{-1}(\omega) - \hat{P}(k,\omega)\hat{t}(k) + \hat{\Sigma}(k,\omega) \right]^{-1} \hat{P}(k,\omega)\,. \tag{8}$$

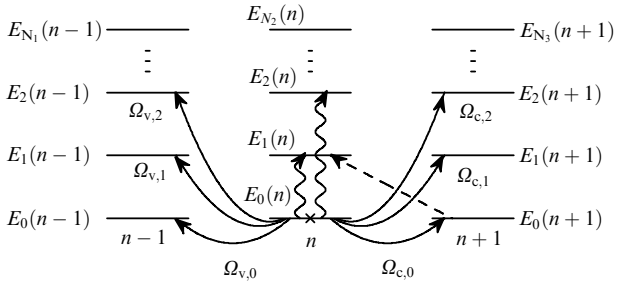

Figure 1. Hilbert space of exact eigenstates for the MeO_6 cluster. Ground term with n electrons at $T = 0$ is marked with an $\times$, while the excited terms are empty. Terms with an electron removed (a hole created) with $n-1$ electrons and terms with $n+1$ electrons (an electron added) are not filled. Various Fermi-type excitations, shown by solid arrows, correspond to Hubbard fermions of the valence band $\Omega_{v,i}$ and the conduction band $\Omega_{c,i}$. Vertical wavy lines correspond to local excitons. Dashed arrow shows the creation of a hole from an unfilled term $E_0(n+1)$ into an unfilled excited state $E_1(n)$; the corresponding quasiparticle has zero spectral weight at $T = 0$ but acquires a nonzero spectral weight at finite temperatures, proportional to the population of the excited state [56].

Here, $\hat{\Sigma}(k,\omega)$ and $\hat{P}(k,\omega)$ are the respective mass and force operators, and $G_{0mn}(\omega) = \delta_{mn}[1/(\omega - \Omega_m)]$. In Eqn (8), an additional quantity appears that was absent in the standard diagram technique for Fermi/Bose particles, the force operator $\hat{P}(k,\omega)$, which determines the oscillator strength (spectral weight) of the quasiparticles. Thus, similarly to the Lehmann representation, an electron is a linear combination of excitations between different many-electron terms. Such electrons were called Hubbard electrons in the GTB approach to emphasize their difference from free electrons.

In the Hubbard-I approximation, the structure of the exact Green's function (8) is preserved, but the mass operator is set equal to zero and the force operator is replaced as $P_{mn}(k,\omega) \to \delta_{mn}F_m$, with $F_m = \langle X^{p,p}\rangle + \langle X^{q,q}\rangle$ being the sum of the occupation numbers of the initial and final multielectron terms. That is why the transitions due to excitation from an unfilled to an unfilled state in Fig. 1 correspond to a quasiparticle with a definite energy but zero spectral weight. In this approximation, the dispersion equation for the spectrum of the Hubbard fermion quasiparticles

$$\det\left|\left|\frac{\delta_{mn}(\omega - \Omega_m)}{F_m} - t_{mn}(k)\right|\right| = 0 \qquad (9)$$

is similar to the standard tight-binding equation: it also involves local energies on the matrix diagonal and an interatomic hopping matrix, but the hopping matrix elements are multiplied by the force operator components, which explains the term 'generalized tight-binding approximation.'

If we restrict ourselves to considering low-energy excitations, then it suffices to keep only the main term in Fig. 1 for each of the three Hilbert-space sectors. As a result, we obtain an effective Hubbard model in which the counterpart of the one-electron configuration is the electrically neutral term d^n, the counterpart of the vacuum state is the hole term d^{n-1}, and the counterpart of the two-electron term is the electron term d^{n+1}. In the usual Hubbard model, the parameter is $U = E_0 + E_2 - 2E_1$, and, in the generalized Hubbard model, the effective parameter arises in the form

$$U_{\text{eff}}(d^n) = E_0(d^{n+1}) + E_0(d^{n-1}) - 2E_0(d^n). \qquad (10)$$

Examples of the application of the multiband p–d model and the effective Hubbard model for the analysis of SCOs in specific transition-metal compounds are given in Sections 4–7.

3.3 Interatomic exchange interaction with excited cation terms taken into account

In magnetic insulators, the main exchange interaction mechanism is known to be superexchange via nonmagnetic anions [59, 60]. In a simplified version of a magnetic insulator based on the Hubbard model, there are formally no oxygen ions, but the interatomic cation–cation hopping parameter t is due to p–d cation–anion hops in the second order of the perturbation theory. In the strongly correlated regime, the presence of the lower and upper Hubbard bands leads to the appearance of a 2×2 hopping matrix. Its diagonal elements t_{11} and t_{22} determine the dispersion of the lower and upper Hubbard bands, and the off-diagonal elements $t_{12} = t_{21}$ describe interband interatomic hops. Eliminating them from the effective Hamiltonian in the second order of the perturbation theory leads to the antiferromagnetic (AFM) superexchange interaction $J = 2t^2/U$ [61–63]. In fact, the exchange interaction in the Hubbard model forms as a result of the creation and subsequent annihilation of a virtual electron–hole pair.

Usually, in the theory of magnetism, the exchange interaction between the ground-state terms of the cation is taken into account under the assumption that the other excited terms lie much higher in energy (on the scale of the exchange interaction J). This assumption is usually justified, but in the situation with SCOs, when a term is located high at a low pressure but intersects the former ground term at the crossover point, the possible contribution of the excited term to the exchange interaction must be taken into account. Another situation that requires taking the contribution from the excited term to the exchange interaction into account arises in experiments with femtosecond pumping of selected d–d transitions. Just this case occurs under pulsed pumping of the forbidden transition from the $^6A_1$ state of Fe^{3+} to the excited $^4T_2$ state in $FeBO_3$ single crystals [64]. Because the initial state has spin $S = 5/2$ and the excited state has spin $S = 3/2$, this transition can be considered a dynamical SCO. The essence of the crossover is not the crossing of energy levels observed in static experiments but the change in the population of different spin states, which can also be induced by external pumping. In Section 2, we mentioned the LIESST effect, which also causes a dynamical SCO.

In the GTB approach, interatomic hopping terms, as can be seen from the structure of the electron creation and annihilation operators in (7), are bilinear products of the Hubbard X operators, and hence we actually have a multiband analogue of the Hubbard model. Therefore, in the X-representation, we can obtain expressions for the effective Heisenberg-type Hamiltonian in the form of a sum of partial contributions with all virtual electron–hole pairs, including those involving excited terms, taken into account. In this way, we can go beyond the traditional description of the exchange interaction in the theory of magnetism where the contributions of the excited terms are ignored [65–67]. It turns out that, in the case of a 180-degree exchange with nonzero cation–anion–cation hopping parameters t_σ and t_π, the sign

of the partial contribution to the total exchange is determined by a simple rule: if the spins of the hole term d^{n-1} and the electronic term d^{n+1} are different, then the interaction has the ferromagnetic sign. For the same spins of the hole and electron terms, the interaction is antiferromagnetic. Previously, the same rule was obtained for the exchange between the ground-state terms [68, 69].

3.4 Two-band Hubbard–Kanamori model in the representation of Hubbard's *X* operators. Exciton phase in the vicinity of the SCO

In this section, we consider the minimal generalization of the Hubbard model that allows studying the SCO. This is the two-band Hubbard–Kanamori model, which includes two single-electron orbitals with energies ε_1 and ε_2, the intraatomic Coulomb interactions, and interatomic hopping. The Hamiltonian of the model can be written as

$$\hat{H} = \hat{H}_{\Delta} + \hat{H}_t + \hat{H}_{\text{Coulomb}} \,. \tag{11}$$

The first term on the right-hand side of (11) describes two one-electron states with energy levels ε_1 and $\varepsilon_2 = \varepsilon_1 + \Delta$, where Δ is the energy of electrons in the crystal field (for convenience, we can set $\varepsilon_1 = 0$),

$$\hat{H}_{\Delta} = \varepsilon_1 \sum_{i,\sigma} a^{\dagger}_{i,1,\sigma}\, a_{i,1,\sigma} + \varepsilon_2 \sum_{i,\sigma} a^{\dagger}_{i,2,\sigma}\, a_{i,2,\sigma} \,.$$

The second term contains interatomic hopping, both intraband t_1 and t_2, and the interband terms t_{12}:

$$\hat{H}_t = t_1 \sum_{\langle i,j\rangle} a^{\dagger}_{1i} a_{1j} + t_2 \sum_{\langle i,j\rangle} a^{\dagger}_{2i} a_{2j} + t_{12} \sum_{\langle i,j\rangle} (a^{\dagger}_{2i}\, a_{1j} + a^{\dagger}_{1i}\, a_{2j}) \,. \tag{12}$$

In the Kanamori approximation [70], local interactions can be written as

$$\begin{aligned}\hat{H}_{\text{Coulomb}} = {} & U \sum_{i,\lambda} a^{\dagger}_{i\lambda\uparrow} a^{\dagger}_{i\lambda\downarrow} a_{i\lambda\uparrow} a_{i\lambda\downarrow} + V \sum_{i,\lambda\neq\lambda'} a^{\dagger}_{i\lambda\uparrow} a^{\dagger}_{i\lambda'\downarrow} a_{i\lambda\uparrow} a_{i\lambda'\downarrow} \\ & + V \sum_{i,\lambda>\lambda',\sigma} a^{\dagger}_{i\lambda\sigma} a^{\dagger}_{i\lambda'\sigma} a_{i\lambda\sigma} a_{i\lambda'\sigma} + J_{\text{H}} \sum_{i,\lambda>\lambda',\sigma} a^{\dagger}_{i\lambda\sigma} a^{\dagger}_{i\lambda'\sigma} a_{i\lambda'\sigma} a_{i\lambda\sigma} \\ & + J_{\text{H}} \sum_{i,\lambda\neq\lambda'} a^{\dagger}_{i\lambda\uparrow} a^{\dagger}_{i\lambda'\downarrow} a_{i\lambda'\uparrow} a_{i\lambda\downarrow} + J' \sum_{i,\lambda\neq\lambda'} a^{\dagger}_{i\lambda\uparrow} a^{\dagger}_{i\lambda\downarrow} a_{i\lambda'\uparrow} a_{i\lambda'\downarrow} \,.\end{aligned} \tag{13}$$

The Coulomb interactions include intraorbital U and interorbital V repulsions, as well as the J_{H} Hund exchange and the J' interband pair exchange terms. The magnitude of the crystal field depends on the pressure. Because the cation–anion distance decreases when the sample is compressed, the crystal field parameter increases with increasing pressure. At pressures below 100 GPa, typical of SCOs, the crystal field is linearly related to the pressure [71]. An important feature of such a two-orbital model is the possibility of the formation of various localized many-electron (two-particle) states (terms) in the case of half-filling (with the average number of electrons per crystal lattice site $N_{\text{e}} = 2$) in the zeroth approximation in the interstitial hopping $t_{\lambda\lambda'} = 0$. Such states have spins $S = 0, 1$ (Fig. 2) and experience a crossover as Δ increases. For $N_{\text{e}} = 2$, the exact diagonalization of the Hamiltonian $\hat{H}_{\Delta} + \hat{H}_{\text{Coulomb}}$ gives six eigenstates. In the range $\Delta < \Delta_{\text{C}}$, the ground state is given by a triplet ($S = 1$) HS state $|\sigma\rangle$ with energy $E_{\text{HS}} = 2\varepsilon_1 + \Delta + V - J_{\text{H}}$ (see the red line in Fig. 2), which is triple-degenerate in the spin projection

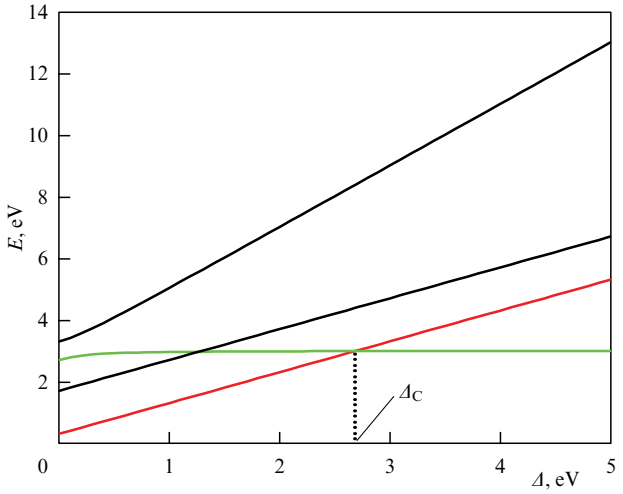

Figure 2. Dependence of term energies on crystal field Δ. Red line shows the position of the HS state ($S = 1$), and the green line, the position of the LS state ($S = 0$). Black lines are excited singlet states and Δ_{C} is a crossover point. Calculations were performed with the following set of Coulomb interaction parameters: $U = 3$, $V = 1$, $J_{\text{H}} = 0.7$, and $J' = 0.3$ (all energies are expressed in electronvolts) [72].

$\sigma = 0, \pm 1$,

$$|\sigma\rangle = \begin{cases} a^{\dagger}_{1\uparrow} a^{\dagger}_{2\uparrow} |0\rangle \,, & \sigma = +1 \,, \\ \dfrac{1}{\sqrt{2}} \left(a^{\dagger}_{1\uparrow} a^{\dagger}_{2\downarrow} |0\rangle + a^{\dagger}_{1\downarrow} a^{\dagger}_{2\uparrow} |0\rangle \right) , & \sigma = 0 \,, \\ a^{\dagger}_{1\downarrow} a^{\dagger}_{2\downarrow} |0\rangle \,, & \sigma = -1 \,, \end{cases}$$

for $\Delta > \Delta_{\text{C}}$, the ground state is given by the singlet ($S = 0$) LS state $|s\rangle = C_1(\Delta) a^{\dagger}_{1\uparrow} a^{\dagger}_{1\downarrow} |0\rangle - C_2(\Delta) a^{\dagger}_{2\uparrow} a^{\dagger}_{2\downarrow} |0\rangle$ with the energy $E_{\text{LS}} = 2\varepsilon_1 + (\Delta + U) - (\Delta^2 + J'^2)^{1/2}$ (see the green line in Fig. 2). At the crossover point $\Delta = \Delta_{\text{C}} = [(U - V + J_{\text{H}})^2 - J'^2]^{1/2}$, the energy levels cross: $E_{\text{HS}} = E_{\text{LS}}$. The remaining two states are the excited singlet states $|s_1\rangle = 1/\sqrt{2}(a^{\dagger}_{1\uparrow} a^{\dagger}_{2\downarrow} |0\rangle - a^{\dagger}_{1\downarrow} a^{\dagger}_{2\uparrow} |0\rangle)$ and $|s_2\rangle = C_2(\Delta) a^{\dagger}_{1\uparrow} a^{\dagger}_{1\downarrow} |0\rangle + C_1(\Delta) a^{\dagger}_{2\uparrow} a^{\dagger}_{2\downarrow} |0\rangle$, where $C_1(\Delta) = [1 - C_2^2(\Delta)]^{1/2}$ and $C_2(\Delta) = x/2[1 + x + (1 + x)^{1/2}]$ (with $x = J'^2/\Delta^2$) are normalization coefficients (in Fig. 2, these states are shown with black lines).

To derive the effective Hamiltonian, it is convenient to use the Hubbard X operators $X^{p,q} = |p\rangle\langle q|$ [73] constructed from the eigenstates of the Hamiltonian $\hat{H}_{\Delta} + \hat{H}_{\text{Coulomb}}$,

$$(\hat{H}_{\Delta} + \hat{H}_{\text{Coulomb}}) |p\rangle = E_p |p\rangle \,,$$

with different numbers of electrons $N_{\text{e}} = 1, 2, 3$. Because the Hubbard operators form a basis, any local operator can be expressed in terms of a linear combination of X operators, including the one-electron annihilation (creation) operator at site i with orbital index λ and spin projection $\sigma = \pm 1/2$:

$$a_{i\lambda\sigma} = \sum_{p,q} |p\rangle\langle p| a_{i\lambda\sigma} |q\rangle\langle q| = \sum_{p,q} \gamma_{\lambda\sigma}(p,q) X_i^{p,q} \,. \tag{14}$$

Introducing the quasiparticle band index $m \leftrightarrow (p,q)$, we can write $a_{i\lambda\sigma} = \sum_m \gamma_{\lambda\sigma}(m) X_i^m$ and $a^{\dagger}_{i\lambda\sigma} = \sum_m \gamma^*_{\lambda\sigma}(m) X_i^{\dagger m}$.

In the representation of the Hubbard X operators, Hamiltonian (11) has the standard form for the Hubbard model and the GTB approach:

$$\hat{H} = \sum_{i,p} E_p X_i^{p,p} + \sum_{\langle i,j\rangle} \sum_{mn} t_{mn}\, X_i^{\dagger m} X_j^n \,. \tag{15}$$

Here, E_p is the energy of multielectron terms and $t_{mn} = \sum_{\sigma,\lambda,\lambda'} t_{\lambda\lambda'}\gamma^*_{\lambda\sigma}(m)\gamma_{\lambda'\sigma}(n)$ is the renormalized hopping integral. The electron structure of Hubbard fermions in the GTB method is found from dispersion equation (9). Below, we present several possible options for the band structure, but first we need to describe the phase diagram of this model. There are competing magnetic phases: the HS AFM phase and the paramagnetic phase, and an LS nonmagnetic one. In addition, exciton ordering is possible. In the case of SCO, there is a local boson, an exciton whose excitation energy lies between the energies of the ground and excited terms. At the crossover point, the boson energy vanishes, similarly to the soft-mode energy in the theory of phase transitions. Therefore, in the vicinity of the SCO, we can expect the interaction of excitons to lead to their Bose condensation. In semimetals or semiconductors with a narrow band gap, exciton pairing is known to occur due to the Coulomb interaction [74, 75]. In our two-band model, in the atomic limit (at zero interatomic hopping parameters), there already is an exciton: the operator $X^{\sigma,s}$ describes a local transition from an LS singlet to an HS triplet with the spin projection σ. In recent years, many papers have been published on exciton ordering in the regime of strong electron correlations [76–81]. Below, we present the phase diagram of the two-band Hubbard–Kanamori model on the pressure–temperature plane, with the pressure specified via the crystal field.

For this, using the projection properties of the Hubbard operators, we construct an effective Hamiltonian using a unitary transformation that eliminates the off-diagonal hopping components in (15) in the second order. As a result, we obtain the effective Hamiltonian [82]

$$\hat{H}_{\text{eff}} = \hat{H}_S + \hat{H}_{nn} + \hat{H}_{\text{ex}}\,. \tag{16}$$

Here, $\hat{H}_S$ contains the exchange contribution to the Heisenberg Hamiltonian, with the energy of the electron configurations of the LS and HS states taken into account,

$$\hat{H}_S = \frac{1}{2}\,J\sum_{\langle i,j\rangle}\left(\hat{\mathbf{S}}_i\hat{\mathbf{S}}_j - \frac{1}{4}\,\hat{n}_i\,\hat{n}_j\right) + E_{\text{LS}}\sum_i X_i^{s,s} + E_{\text{HS}}\sum_{i,\sigma} X_i^{\sigma,\sigma}\,, \tag{17}$$

where $\hat{\mathbf{S}}_i$ are the spin operators for $S=1$: $\hat{S}_i^+ = \sqrt{2}(X_i^{+1,0} + X_i^{0,-1})$, $\hat{S}_i^- = \sqrt{2}(X_i^{0,+1} + X_i^{-1,0})$, and $\hat{S}_i^z = X_i^{+1,+1} - X_i^{-1,-1}$; the exchange parameter is $J = (t_{11}^2 + 2t_{12}^2 + t_{22}^2)/\Omega_{\text{g}}$, Ω_{g} is the energy of charge transfer between the centers of the upper and lower Hubbard subbands, and $\hat{n}_i = 2(X_i^{s,s} + \sum_\sigma X_i^{\sigma,\sigma}) = 2(\hat{n}_i^{\text{LS}} + \hat{n}_i^{\text{HS}})$ is the particle number operator at a site i ($\hat{n}_i{}^{\text{LS(HS)}}$ is the particle number operator in the LS (HS) state). If we define the spin gap ε_S as the difference $E_{\text{HS}} - E_{\text{LS}}$, then (17) can be represented as

$$\hat{H}_S = \frac{1}{2}\,J\sum_{\langle i,j\rangle}\left(\hat{\mathbf{S}}_i\hat{\mathbf{S}}_j - \frac{1}{4}\,\hat{n}_i\,\hat{n}_j\right) - \varepsilon_S\sum_i X_i^{s,s} + NE_{\text{HS}}\,,$$

where N is the number of crystal lattice sites, with $\varepsilon_S = 0$ corresponding to the SCO in the one-ion approximation (without taking cooperative effects into account).

The second term on the right-hand side of (16) describes the density–density interaction of the LS states,

$$\hat{H}_{nn} = \frac{1}{2}\,\tilde{J}\sum_{\langle i,j\rangle} X_i^{s,s}\,X_j^{s,s}\,, \tag{18}$$

where $\tilde{J} = [1 - (2C_1C_2)^2](t_{11}^2 - 2t_{12}^2 + t_{22}^2)/\Omega_{\text{g}}$.

The last term in (16) contains interatomic hopping of excitons and biexcitons,

$$\hat{H}_{\text{ex}} = \sum_\sigma\sum_{\langle i,j\rangle}\left[\frac{1}{2}\,J'_{\text{ex}}\left(X_i^{\sigma,s}X_j^{s,\sigma} + X_i^{s,\sigma}X_j^{\sigma,s}\right) - \frac{1}{2}\,J''_{\text{ex}}(-1)^{|\sigma|}\left(X_i^{\sigma,s}X_j^{\bar{\sigma},s} + X_i^{s,\sigma}X_j^{s,\bar{\sigma}}\right)\right], \tag{19}$$

where $J'_{\text{ex}} = 2C_1C_2(t_{11}t_{22} - t_{12}^2)/\Omega_{\text{g}}$ and $J''_{\text{ex}} = (t_{11}t_{22} - t_{12}^2)/\Omega_{\text{g}}$.

In the mean-field approximation for a two-sublattice AFM with sublattice magnetizations $m_{\text{A(B)}} = \langle\hat{S}^z_{i_{\text{A(B)}}}\rangle$ and with the exciton order parameter components $\Delta^\sigma_{\text{A(B)}} = \langle X^{s,\sigma}_{i_{\text{A}}(i_{\text{B}})}\rangle$, such that $(\Delta^\sigma)^\dagger = \langle X^{\sigma,s}\rangle = \Delta^\sigma$, the phase diagram is shown in Fig. 3. We note that a deviation of the averages from zero, $\Delta^\sigma \neq 0$, indicates quantum mechanical mixing of the LS and HS states, albeit in the absence of spin-orbit interaction.

Here and hereafter, the temperature and the spin gap are given in units of the exchange integral J. The calculations were performed at $J = 28$ K. In what follows, we use the hopping integral values $t_{11} = t_{22} = 1$ eV and $t_{12} = 0.5$ eV, for which we have $\tilde{J}/J = 0.6$ and $J''_{\text{ex}}/J = 0.3$. Near the SCO, $C_1 \approx 1$ and $C_2 \approx 0$, whence $J'_{\text{ex}} \approx 0$. We can see that $n_{\text{HS,A}} = n_{\text{HS,B}}$ (Fig. 3a, b); $m_{\text{A}} = -m_{\text{B}}$ indicates that the long-range AFM order is realized in the system (Fig. 3c, d); $\Delta^-_{\text{A}} = -\Delta^+_{\text{B}}$ (Fig. 3e, f), while $\Delta^+_{\text{A}} = \Delta^-_{\text{B}} = 0$. As we can see, due to the presence of the cooperative exchange interaction J, the ground AFM HS state is preserved in the system for ε_S up to $\varepsilon_S = \varepsilon_S^{\text{C}} \approx 2J$ (Fig. 3c, d), although the LS state is the ground state in the single-ion picture for $\varepsilon_S > 0$. An increase in the critical value ε_S^{C} due to cooperative effects is quite understandable, because the exchange interaction stabilizes the HS state by decreasing its energy. For $\varepsilon_S > \varepsilon_S^{\text{C}}$, the ground AFM HS state is replaced with a diamagnetic LS state. Near ε_S^{C}, a region of exciton condensate appears that coexists with the long-range AFM order.

In the paramagnetic HS state, as can be seen from Fig. 4b, each band splits into upper and lower Hubbard subbands; for the given model parameters, a semimetallic state is formed. An insulator state appears in the HS AFM phase (Fig. 4a). The semimetal exists in the LS state at high pressures far from the crossover point (Fig. 4d). An exciton AFM insulator is realized near the crossover (Fig. 4c).

4. Effect of SCOs on the electronic structure and physical properties of 3d metal oxides at high pressures

The 3d metal monoxides MnO, FeO, CoO, and NiO were the first materials for which the role of strong correlations in the formation of their electronic properties was elucidated. Peierls and Mott believed that NiO exhibits a deviation from the one-electron band theory, which later led to the concept of Mott insulators [83]. It is expected that at high external pressure, an increase in the width of the electron band leads to an insulator–metal transition (IMT) with the closing of the insulator gap and delocalization of 3d electrons [84] and the collapse of magnetic moments [85] (Fig. 5). In this section, we present the results of calculating the electron structure in the AFM phase, the magnetic moments of the sublattices, and the volume of the crystal at zero temperature in the generalized gradient approximation (GGA) in of DFT, depending on the external pressure. For all oxides except

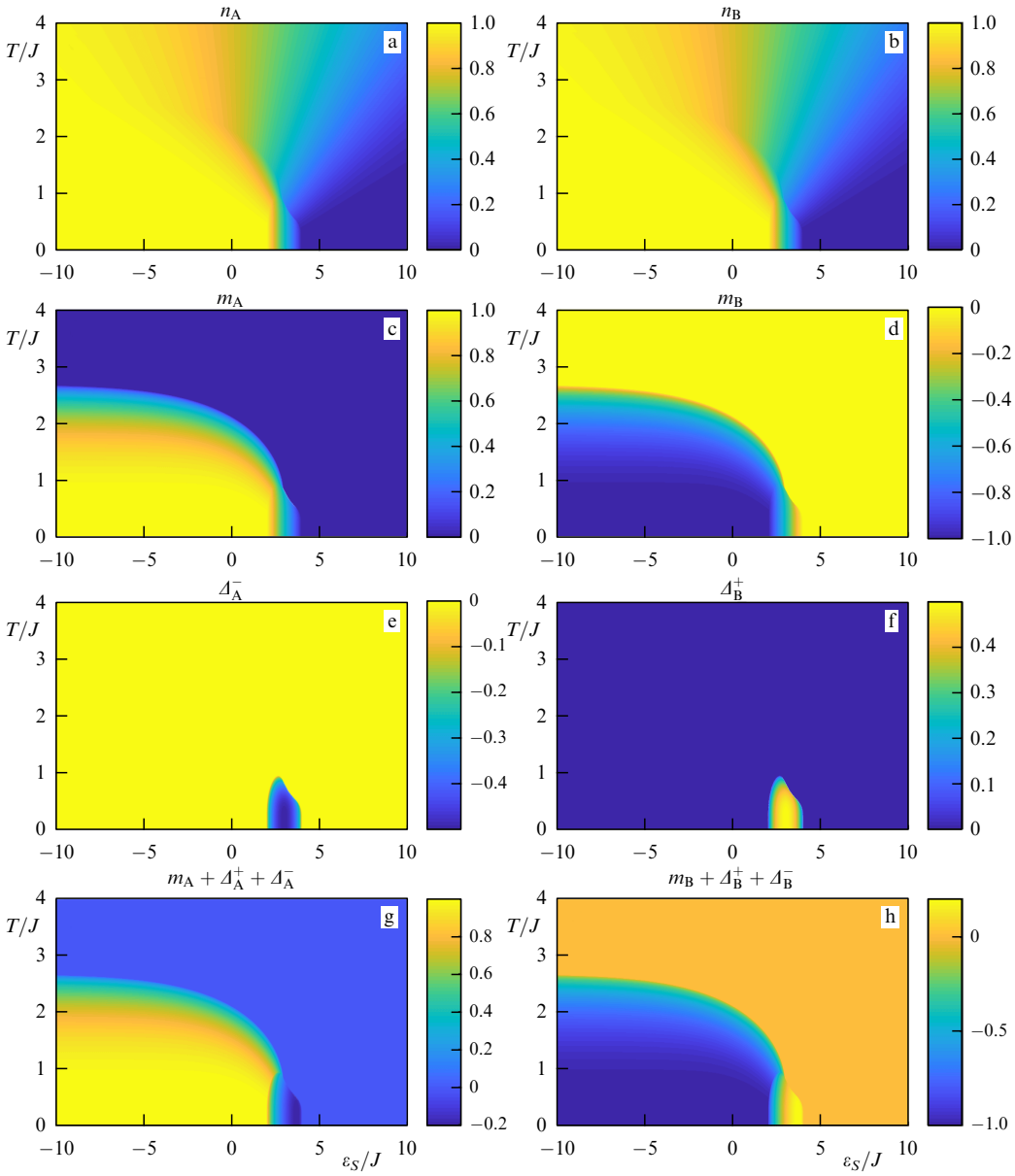

Figure 3. Calculated phase diagrams of (a, b) HS state population n, (c, d) magnetization m, (e, f) components of the exciton order parameter Δ, and (g, h) sum $m + \Delta$ for two sublattices: A (a, c, e, g) and B (b, d, f, h) [82].

NiO, the SCO was found at pressures up to 250 GPa. Metallization and magnetic collapse are known, for example, at pressures above 70 GPa in FeO [85, 86], from 80 to 100 GPa in MnO [87, 88], and above 120 GPa in CoO [89, 90]. So far, it has been established that NiO is stable at pressures up to 147 GPa [91], and no magnetic collapse has been found in NFS of synchrotron radiation at pressures up to 280 GPa [92].

Below, we consider the SCO and its effect on the electronic structure and properties of individual oxides. We note that, according to LDA + DMFT calculations [93], the SCO in Fe_2O_3 is accompanied by an IMT at pressures of about 50 GPa. As the volume decreases, the calculation results show a first-order phase transition and suppression of the charge gap in the electron spectrum. Similarly, for the classical Mott insulator MnO, LDA + DMFT calculations [86], as the pressure increases, reproduce the simultaneous collapse of the magnetic moment and volume, and the IMT.

4.1 Monoxides MnO, FeO, CoO, and NiO

4.1.1 MnO. As a typical representative of Mott insulators, MnO with the B1 structure and a half-filled 3d shell is of great interest for both experimental and theoretical studies. A structural transition under impact loading [94] and according to Raman spectral measurements [95] was found in the pressure range of 95–105 GPa. As a result of a combination of transport [96], magnetic [96], and spectroscopic [87, 88] measurements, it was established that a first-order Mott IMT occurs in the pressure region of 100 GPa with a jump in volume from $V/V_0 = 0.68$ to 0.63, attended by a collapse of the magnetic moment from $5\mu_B$ to $1\mu_B$. Such a change is just expected at the SCO from an HS $S = 5/2$ to an LS $S = 1/2$ term. As shown by LDA + DMFT calculations [86], the transition mechanism is associated with an increase in the crystal field, rather than the broadening of the electron band expected in the Hubbard model

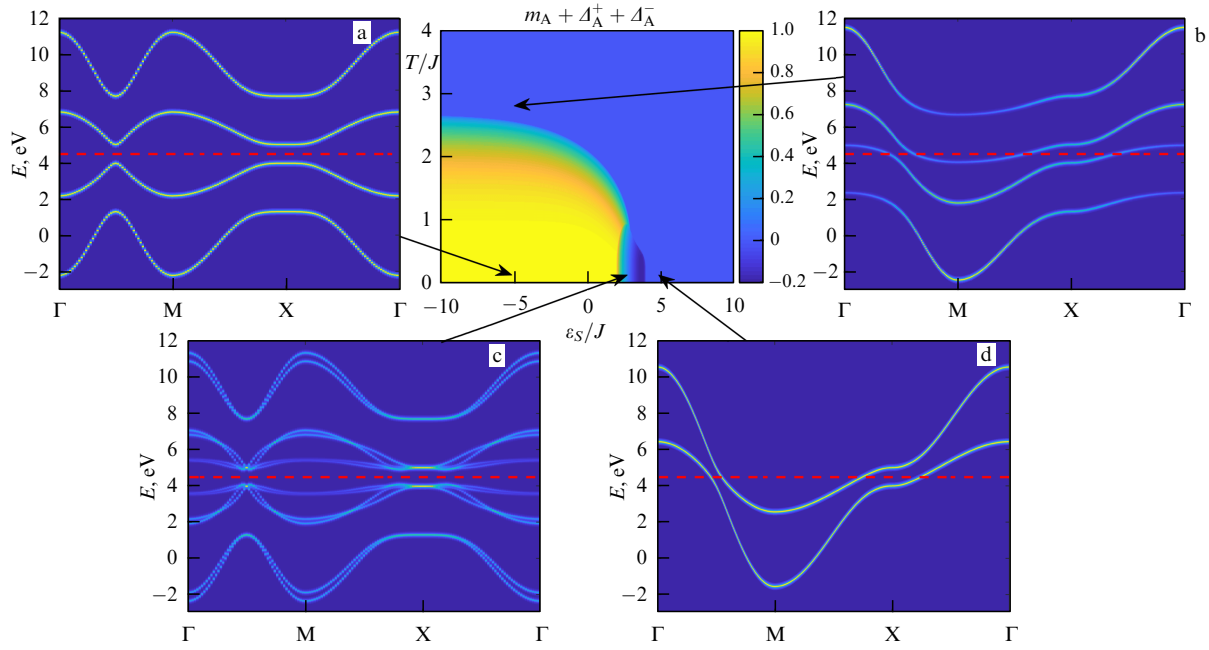

Figure 4. Electron structure of the two-band Hubbard–Kanamori model and its relation to the phase diagram in the pressure–temperature plane [82]. Fermi level is shown with the red dashed line.

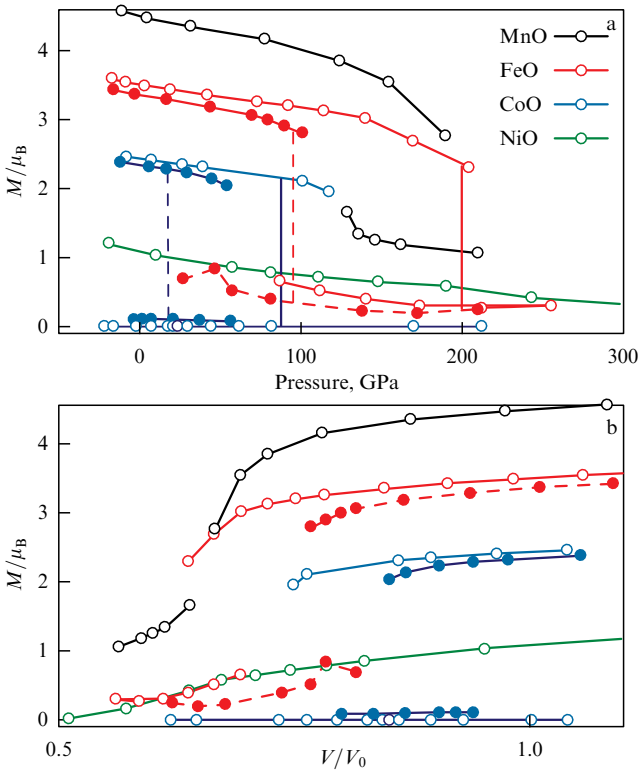

Figure 5. Magnetic moments expressed in Bohr magnetons μ_B for AFM oxides with the B1 structure as a function of (a) pressure and (b) relative volume for MnO, FeO, CoO, and NiO. Vertical straight lines in (a) show the transition pressure [85].

framework. The change in the populations of d-orbitals from $t_{2g}^3 e_g^2$ to e_g^5 obtained in the calculations in [86] corresponds to a simple pattern of intersection of the terms of the HS ($S = 5/2$) and LS ($S = 1/2$) ionic states of Mn^{2+}.

4.1.2 FeO. The properties shown by FeO under pressure have been investigated both experimentally and theoretically. Under normal conditions, FeO crystallizes into a cubic NaCl-type B1 structure and transforms into a rhombohedrally distorted rB1 structure at pressures above 16 GPa [97]. A further increase in pressure leads to a transition to an NiAs-type B8 structure at pressures above 90 GPa and a temperature of 600 K [98]. The SCO in FeO has been observed by different authors, giving different data on the critical pressure value. According to Mössbauer spectroscopy measurements [99], the SCO occurs at a pressure of 90 GPa. At the same time, according to XES, the HS state exists at room temperature, at least at pressures up to 143 GPa [17]. The LS state was observed at 140 GPa upon laser heating [100]. However, in all studies [17, 99, 100], there was no simultaneous structural control. In a later study [101], the appearance of an NiAs-type structure at a pressure above 140 GPa was shown. According to theoretical calculations [102], the structural transition into the NiAs lattice controls the appearance of metallic properties of FeO. We note that, for the d^6 configuration, the HS state spin is $S = 2$, while the LS state spin vanishes, $S = 0$. Simultaneous measurement of the spin state from XES synchrotron data and the structure from X-ray diffraction (XRD) data have allowed establishing the FeO phase diagram shown in Fig. 6.

The insulator properties of the HS state and metallic properties of the LS state have been confirmed by optical [104] and transport [105] measurements. Theoretical GGA + DMFT calculations of the electronic structure of FeO [105] at high pressures and a temperature of 300 K showed the existence of an insulator state at pressures $P = 0$ and $P = 68$ GPa (Fig. 7a, b). At a high temperature, 2000 K, and a low pressure, $P = 13$ GPa, a pseudogap is formed (the state of a poor metal) (Fig. 7c). With a further increase in pressure, the gap closes, and an LS metal exists at $P = 88$ GPa (Fig. 7d).

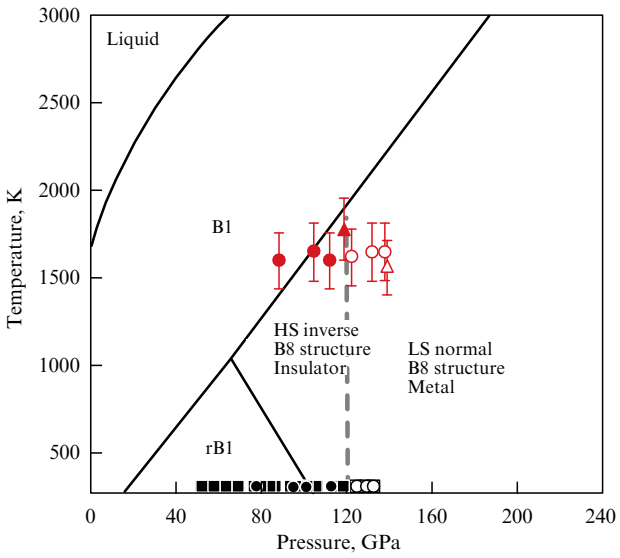

Figure 6. Phase diagram of FeO. Filled and empty symbols, respectively, show the HS inverse and LS normal structures of B8 [103].

4.1.3 CoO. We consider the SCO and metallization in CoO, where structural phase transitions are observed at pressures up to 150 GPa: from the cubic Cube I phase to the orthorhombic Rhombo I phase at pressure $P_{C1} = 43$ GPa with no change in volume, from the Rhombo I to Rhombo II phase at $P_{C2} \sim 90$ GPa with a 2.7% change in volume, and the return to the Cube II phase at $P_{C3} \sim 120$ GPa [89, 90]. The electrical resistance as a function of pressure exhibits a sharp decrease (jump by eight orders of magnitude) in the pressure range of 43–63 GPa, a break at $P = 80$ GPa, and a metallic behavior at $P = 133$ GPa [90]. The authors of [90] discuss the possibility of spin collapse in the range $P = 80$–90 GPa, based largely on calculations [85]. We did not find direct experimental evidence of the SCO in CoO in the literature. Therefore, we theoretically consider the features of the IMT and SCO mechanisms and their possible interrelation in CoO in the framework of the many-electron approach [106, 107]. Previously, in [107], it was shown that, in the general case, SCO can change the value of the effective parameter of electron correlations, in particular, attenuate them for the d^5 configurations. Enhancement of correlation effects for d^6 configurations and the properties of IMTs under pressure

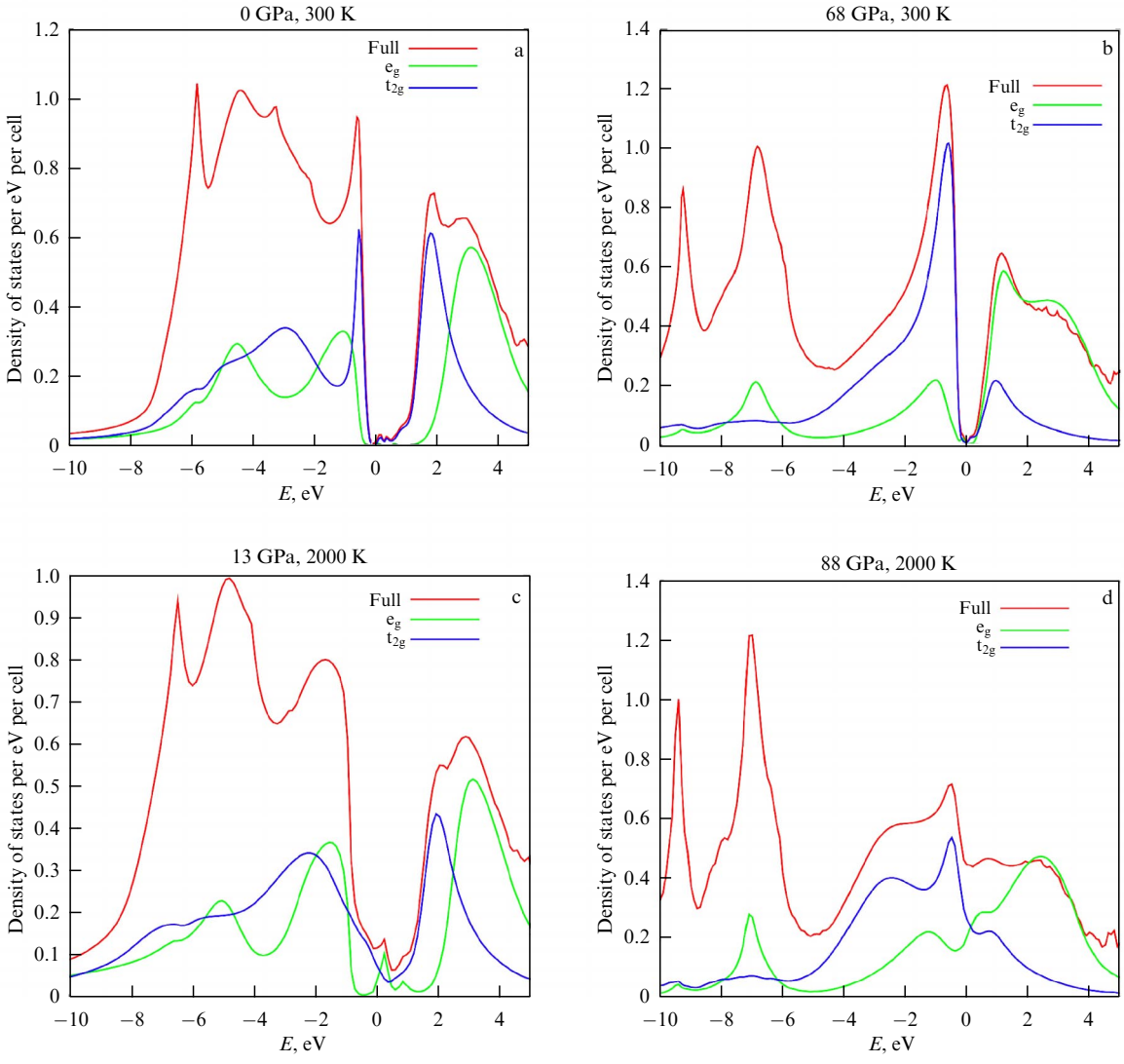

Figure 7. Density of states of FeO at two temperatures and different pressures. Dielectric state is observed at $T = 300$ K and pressures (a, b) $P = 0$ and $P = 68$ GPa. At $T = 2000$ K, (c) a pseudogap (poor metal state) is formed at $P = 13$ GPa and (d) a metallic state appears at $P = 88$ GPa [105].

are considered in [106]. In the framework of the same approach, it turns out that, for the Co^{2+} ion in the d^7 configuration, the SCO does not affect the electron correlation parameter. We also discuss possible mechanisms of the influence of pressure on the behavior of electrical resistance.

In the case of CoO with the Co^{2+} ion, two terms compete in the d^7 configuration as the pressure increases:

(a) the HS term with spin $S = 3/2$ and energy

$$E_{\mathrm{HS}}(d^7) = E_{\mathrm{C}}(d^7) - 8Dq - 11J_{\mathrm{H}}\,; \tag{20}$$

(b) the LS term with spin $S = 1/2$ and energy

$$E_{\mathrm{LS}}(d^7) = E_{\mathrm{C}}(d^7) - 18Dq - 9J_{\mathrm{H}}\,. \tag{21}$$

Here, $E_{\mathrm{C}}(d^7)$ is the spin-independent part of the Coulomb interaction for seven electrons in the Co^{2+} ion and J_{H} is Hund's exchange parameter. The $10Dq$ crystal field increases as the pressure increases, and we approximate its dependence as $10Dq(P) = 10Dq(0) + \alpha_{\Delta} P$ [71]. It can be seen from Eqns (20) and (21) that, for a free ion in a zero field of the crystal, the HS state is more favorable, but with an increase in the crystal field, the energy of the LS state decreases faster and the energies equalize when the condition $10Dq = 2J_{\mathrm{H}}$ is satisfied, which occurs at pressure

$$P_S = \frac{2J_{\mathrm{H}} - 10Dq(0)}{\alpha_{\Delta}}\,.$$

To calculate the dependence of effective Hubbard parameter (10) on pressure, we must write the energies of the HS and LS terms of the d^6 configuration with one hole and the d^8 configurations with one added electron, similarly to Eqns (20) and (21). These energies are given in [107], whence, both below and above the crossover,

$$U_{\mathrm{eff}}(d^7) = U - J_{\mathrm{H}}\,. \tag{22}$$

Thus, the Coulomb part of the insulator gap for CoO is independent of pressure, in contrast to the case of oxides with d^5 and d^6 ions [108]. In the regime of strong correlations, the Mott–Hubbard gap can be estimated as

$$E_{\mathrm{g}} = U_{\mathrm{eff}} - W\,. \tag{23}$$

Because the band half-width $W = zt$, where z is the number of nearest neighbors and t is the hopping integral between nearest neighbors, is also independent of the spin state, we conclude that the SCO and the IMT in CoO are independent [108]. To analyze the dependence of electrical resistance on pressure, it is necessary to take the dependence of the band width on pressure into account, which can be represented as $W(P) = W(0) + \alpha_W P$, leading to the following formula for the energy of the insulator gap:

$$E_{\mathrm{g}}(P) = U - J_{\mathrm{H}} - W(0) - \alpha_W P\,.$$

The structural transition from the cubic Cube I phase to the orthorhombic Rhombo I phase at pressure $P_{\mathrm{C1}} = 43$ GPa can change the band width by δW due to orthorhombic distortion. As a result, above the transition point in the Rhombo I phase, the insulator gap can be written as $E_{\mathrm{g}}(P) = U - W(0) - \alpha_W P - \delta W$. Because no information was given in [109] regarding the presence of impurities and the conduction mechanism, we can assume activation conduction to operate with activation energy $E_{\mathrm{a}} = 0.5E_{\mathrm{g}}$. Then, from the jump in the resistance by eight orders of magnitude at $P_{\mathrm{C1}} = 43$ GPa at room temperature, we can estimate the jump in the gap as $\delta W \approx 0.5$ eV. The remaining parameters involved in Eqn (23) at zero pressure ($U_{\mathrm{eff}} = U - J_{\mathrm{H}}$ and $W(0) = 6t_0$) were estimated in [108] from the Néel temperature $T_{\mathrm{N}} = 290$ K [110] using the results of parameter calculations in the DFT framework [111]. Using the constrained DFT method, the authors of [111] obtained $U = 5.1$ eV and $J_{\mathrm{H}} = 0.9$ eV for CoO. Calculations of the insulator gap E_{g} in the same paper within various approximations give the following values for CoO: 2.21 eV (LDA + U), 2.47 eV (LDA + U + correlation corrections in the nonself-consistent G_0W_0 method), and 2.54 eV (LDA + U + correlation corrections in the partially selfconsistent GW_0 method). The values of the band gap for CoO measured by photoelectron spectroscopy are 2.5 ± 0.3 eV [112, 113], by X-ray spectroscopy (XAS + XES), 2.6 eV [114], and, according to optical absorption spectra, 2.5 eV [115]. In subsequent calculations, we therefore use the value of the gap at zero pressure $E_{\mathrm{g}}(0) = 2.5$ eV.

To estimate the interatomic hopping integral t_0 in the absence of external pressure, we can use the expression for the interatomic effective Heisenberg exchange interaction J according to the Kramers–Anderson superexchange mechanism in the Hubbard model,

$$J = 2\,\frac{t_0^2}{U_{\mathrm{eff}}} = 2\,\frac{t_0^2}{U - J_{\mathrm{H}}}\,.$$

The value of J can be estimated in terms of the Néel temperature in the mean-field approximation as $T_{\mathrm{N}} = (1/3)JzS(S+1) = 7.5J$. Using the experimental values of the insulator gap 2.5 eV and $T_{\mathrm{N}} = 290$ K, we find $t_0 = 0.076$ eV and $U - J_{\mathrm{H}} = 3$ eV. As a result, with the Hund exchange $J_{\mathrm{H}} = 1$ eV (close to the value of 0.9 eV in [111]), the authors of [108] obtained the Hubbard parameter $U = 4$ eV, which agrees well with the values in [111]. Based on the known values of the Hund exchange integral of 1 eV and the crystal field of $10Dq(0) = 0.7$ eV [113], assuming that the baric derivative of α_{Δ} for CoO is close to the corresponding parameter for $FeBO_3$, $\alpha_{\Delta} = 0.018$ eV GPa^{-1}, we can estimate the SCO pressure as $P_S = 72$ GPa, which is close to the spin collapse values due to the calculation in [85]. The difference in the ionic radii for the HS and LS states of about 10% usually leads to an isostructural transition, also with a large change in volume. The situation for CoO is complicated by the presence of several structural phase transitions, which is probably why the transition in the pressure range of 80–90 GPa, which the authors of [109] attribute to the SCO, is accompanied by a rather small (2.7%) change in volume. Taking the jump in the insulator gap at $P_{\mathrm{C1}} = 43$ GPa into account, the expression for the entire pressure range can be written as

$$E_{\mathrm{g}}(P) = \begin{cases} E_{\mathrm{g}}(0) - \alpha_W P, & P < P_{\mathrm{C1}}\,, \\ E_{\mathrm{g}}(0) - \delta W - \alpha_W P, & P > P_{\mathrm{C1}}\,. \end{cases}$$

The only unknown parameter, the pressure derivative of the gap α_W, can be estimated from the condition $E_{\mathrm{g}}(133\ \mathrm{GPa}) = 0$, which gives $\alpha_W = 0.015$ eV GPa^{-1}. The resulting dependence of electrical resistance on pressure in [108] is in qualitative agreement with the experimental curve in [109]. Near the IMT point, the behavior of the system can

be more complex [116], but here we restrict ourselves to only a qualitative picture. We emphasize that the dependences of the electronic and magnetic properties of CoO on pressure, compared with similar dependences for other transition-metal oxides, have both common features (metallization with increasing pressure, the transition from an HS state to an LS state) and specific differences, primarily weak correlation of the SCO and the IMT. For iron compounds with Fe^{3+} ions in the d^5 configuration and Fe^{2+} ions in the d^6 configuration, the crossover directly affects the Coulomb component of the insulator gap. For CoO, as shown in [108], the Coulomb part of the gap does not change at the crossover point. Generally speaking, due to a change in the volume at the crossover point, the value of the band width can change, and this is an alternative mechanism for the effect of the SCO on the insulator gap.

4.1.4 NiO. At normal pressure, the electron structure of NiO according to LDA + DMFT calculations is in good agreement with the experimental data [117, 118]. As regards the behavior with increasing pressure, NiO exhibits two differences from other monoxides such as MnO, FeO, and CoO. First, there is no SCO for d^8 ions, according to the Tanabe–Sugano diagrams. Second, NiO is the only monoxide that preserves its insulator properties at the currently available pressures. So far, it has been established that NiO is stable at pressures up to 147 GPa [91], and no magnetic collapse has been found in the NFS of synchrotron radiation at $P < 280$ GPa [92]. Nevertheless, the SCO manifests itself rather unexpectedly in the NiO properties at high pressures [119]. The point is that the value of the effective Hubbard parameter $U_{\rm eff}$, Eqn (10), is determined by the energy of not only the neutral term (d^8 in that case) but also the hole term d^7 and the electron term d^9; for the d^7 hole term, the SCO is possible under the condition $10Dq = 2J_{\rm H}$. The HS and LS terms for the d^7 configuration are given in the foregoing, Eqns (20) and (21).

For the d^8 and d^9 configurations, the energies of the ground-state terms are

$$E(d^8) = E_{\rm C}(d^8) - 12Dq - 13J_{\rm H}\,, \tag{24}$$

$$E(d^9) = E_{\rm C}(d^9) - 6Dq - 16J_{\rm H}\,. \tag{25}$$

Finally, for pressures below and above the crossover pressure P_S, $U_{\rm eff}(P)$ can be represented as

$$U_{\rm eff} = \begin{cases} U(8) + 10Dq - J_{\rm H}, & P < P_S\,, \\ U(8) + J_{\rm H}, & P > P_S\,, \end{cases}$$

where $U(8) = E_{\rm C}(d^9) + E_{\rm C}(d^7) - 2E_{\rm C}(d^8)$ is a pressure-independent contribution. The pressure-dependent insulator gap (23) can be written as

$$E_{\rm g}(P) = \begin{cases} U(8) - J_{\rm H} + \Delta_0 - W(0) + (\alpha_\Delta - \alpha_W)P, & P < P_S\,, \\ U(8) + J_{\rm H} - W(0) - \alpha_W P, & P > P_S\,. \end{cases} \tag{26}$$

Here, we introduce the notation $10Dq(P=0) = \Delta_0$. Equation (26) shows that an increase in the crystal field at a low pressure below the SCO leads to an increase in the insulator gap, while an increase in the band width leads to a decrease in the gap for all pressures. Thus, the HS–LS crossover for compounds with d^8 ionic states competes with the tendency to the IMT with increasing pressure. With a further increase in pressure, depending on the relation between the two baric derivatives, α_Δ and α_W, either the initial increase in the gap changes to a decrease or the gap initially decreases monotonically. In both cases, however, the gap has a kink at the SCO pressure P_S in the unoccupied d^7 configuration.

Some parameters in (26) are known from the literature. For example, the crystal field in the absence of external pressure $\Delta_0 = 0.08$ Ry $= 1.08$ eV was found from optical absorption spectra [120, 121], and its baric derivative $\alpha_\Delta = 7.28$ meV GPa^{-1} was taken from optical pressure-dependent spectra [122]. The half-width of the electron band $W(0)$ and the Coulomb parameters U and $J_{\rm H}$ were estimated based on the analysis of experimental data in [123]. Additional fitting of these parameters using the pressure-dependent optical absorption spectra of NiO given in [124] gave the following results: $U(8) = U = 5.45$ eV, $J_{\rm H} = 0.75$ eV, and $W(0) = 1.8$ eV.

With these parameters, the SCO pressure $P_S = 57.7$ GPa is very close to the kink pressure of 55 GPa in the gap $E_{\rm g}$ measured in [124]. The only unknown parameter in (26) is the baric derivative of the band width, α_W; below, we discuss how to use the baric dependence of the Néel temperature $T_{\rm N}(P)$ [125], with $dT_{\rm N}/dP = 7.33$ K GPa^{-1}, to estimate α_W. For NiO, according to Anderson's theory [126], the 180° AFM superexchange interaction of the nearest magnetic cations is $J = 2t^2/U_{\rm eff}$, where t is the cation–anion–cation interatomic electron hopping parameter, which determines the band half-width $W(0) = 6t_0$. At $W(0) = 1.8$ eV, we have $t_0 = 0.3$ eV. For NiO, the 90° nearest-neighbor exchange is negligible and can be omitted. At $P = 0$, in the mean-field approximation for the effective Heisenberg model with the exchange interaction J, $S = 1$, and the number of second neighbors $z_2 = 6$, the Néel temperature can be represented as

$$T_{\rm N}(0) = \frac{1}{3}S(S+1)Jz_2 = \frac{8t_0^2}{U + J_{\rm H}}\,.$$

The baric derivative of the Néel temperature is

$$\frac{dT_{\rm N}}{dP} = \frac{16t_0}{U + J_{\rm H}}\,\alpha_t\,,$$

where α_t determines the increase in the hopping parameter under pressure, and $t(P) = t_0 + \alpha_t P$. With the above parameters U, $J_{\rm H}$, and t_0 and the experimental value $dT_{\rm N}/dP = 7.33$ K GPa^{-1} measured in [125] at $P < 30$ GPa, we obtain $\alpha_t = 9.47$ K GPa^{-1} $= 0.815$ meV GPa^{-1} [119]. The baric dependence of the band half-width is $\alpha_W = 6\alpha_t = 4.89$ meV GPa^{-1}.

An estimate of the insulator gap as a function of pressure shows that $E_{\rm g}(0) = 3.98$ eV at zero pressure. Due to the larger baric derivative of the crystal field $\alpha_\Delta = 7.28$ meV GPa^{-1} compared to $\alpha_W = 4.89$ meV GPa^{-1}, the gap increases at pressures up to the SCO pressure P_S. At the crossover point, $E_{\rm g}(P_S) = 4.12$ eV. The estimate obtained from the pressure dependence of the gap, 2.39 meV GPa^{-1} [119], can be compared with the experimental value of 2.78 ± 0.3 meV GPa^{-1} in Fig. S5 in the appendix in [124]. Above the SCO, the insulator gap decreases with the derivative $\alpha_W = -4.89$ meV GPa^{-1}, which can be compared with the experimental value of -5 ± 0.3 meV GPa^{-1} [124]. Assuming the same linear trend, we estimate the IMT pressure as $P_{\rm IMT} = 900$ GPa. We note that the linear extrapolation of the pressure dependences of the crystal field and the half-

width of the electron band, which is valid at pressures up to 240 GPa (the linear dependence of the gap was measured in [124] at $P \leqslant 240$ GPa), is questionable at higher pressures. Therefore, with a further increase in pressure, it is preferable to use another estimate of the band width and pressure of the IMT, based on the Birch–Murnaghan equation of state [119]. It is known that the interatomic hopping parameter for d electrons depends on the interatomic distance as $t \sim r^{-5}$ [127]. We write the last relation as a function of volume,

$$t(P) = t_0 \left(\frac{V}{V_0} \right)^{-5/3}, \tag{27}$$

where t_0 and V_0 are the hopping parameter and the volume in the absence of external pressure. The volume and pressure are related by the equation of state, or the Birch–Murnaghan equation. Introducing the dimensionless volume $u = V/V_0$, we can represent the Birch–Murnaghan equation as

$$P = \frac{3}{2} B_0 \left[u^{-7/3} - u^{-5/3} \right] \left\{ 1 - \frac{3}{4}(4 - B')(u^{-2/3} - 1) \right\}.$$

Introducing a new variable $x(P) = (V/V_0)^{-5/3}$, we can write the equation for the critical IMT pressure as

$$E_g(P_{IMT}) = U + J_H - W_0 x(P_{IMT}) = 0.$$

The value of the critical pressure is to be found from the condition $x(P_{IMT}) = (U + J_H)/W_0$. We emphasize that this condition does not involve linear extrapolation and is suitable for any pressure values. For the set of parameters $U = 5.45$ eV, $J_H = 0.75$ eV, and $W_0 = 1.8$ eV from [124], the critical pressure is determined by the condition $x(P_{IMT}) = 3.44$. For this value of x, from the Birch–Murnaghan equation, we find the critical volume $V/V_0 = 0.47$ and pressure $P/B_0 = 2.34$ at which the IMT occurs. For the values of elastic moduli from [124], $B_0 = 197$ GPa and $B' = 3.4$, we obtain $P_{IMT} = 461$ GPa. Because the values of elastic moduli differ from one author to another, we also present an estimate of the IMT pressure for the parameters $B_0 = 170$ GPa and $B' = 4.35$ from [92]. For these parameter values, $P_{IMT} = 552$ GPa [119]. Thus, metallization of NiO is possible, but at pressures much higher than for other monoxides. Another interesting conclusion from the study of NiO is the manifestation of the SCO in the virtual d^7 term in the form of a kink in the pressure dependence of the insulator gap, which was observed experimentally in [124]. This is a clear manifestation of many-electron effects in the formation of the electron structure of Mott insulators.

4.2 Spin crossover in $FeBO_3$

$FeBO_3$ crystals, which have two AFM sublattices with a small skew angle between them, are a typical example of weak ferromagnets. Such crystals of good quality can be grown with the ^{57}Fe isotope, which is convenient for Mössbauer studies at high pressures (see review [5]). Experimental data on the study of changes in the $FeBO_3$ crystal structure and magnetic properties [20, 128, 129] stimulated the development of many-electron ideas about the SCO [130, 131]. A review of the results of $FeBO_3$ studies at high pressures and femtosecond pumping is given in [132].

The Fe^{3+} ion has the spin $S = 5/2$ in an oxygen octahedron in the HS state, and the spin $S = 1/2$ above the SCO point in the LS state. In the phase diagram on the pressure–temperature plane, the AFM insulator phase is present at pressures below the SCO point $P_S = 47$ GPa and transforms into the paramagnetic HS phase as the temperature increases, with an almost linear increase in the Néel temperature with pressure. Above the SCO, there is a magnetically ordered semiconductor phase at low temperatures and a paramagnetic phase at high temperatures [21].

The magnetic order was determined from measurements of NFS spectra at different pressures and temperatures. The term AFM should here be understood to mean a weak ferromagnet with a slight skew of two AFM sublattices. An insulator and a semiconductor were distinguished by the shift of the optical absorption edge with the increase in pressure from 3 eV in the HS state to 0.8 eV in the LS state [133]. Mössbauer spectroscopy was used to measure the local magnetic field on the nucleus, and therefore the magnetic ordering type above the SCO was not determined in experiments [21]. It could be assumed that the AFM order is preserved, and the jump in the Néel temperature at the SCO qualitatively corresponds to the transition from spin 5/2 to spin 1/2 due to the factor $S(S+1)$ in the expression for T_N in the mean-field approximation. Later, however, in the framework of the orbitally selective method developed in [65] for calculating the superexchange interaction in Mott–Hubbard insulators, the exchange interaction was shown to be antiferromagnetic $FeBO_3$ in the HS state and to change sign and become ferromagnetic in the LS state [66]. This is due to a different set of d orbitals involved in the formation of the superexchange interaction via oxygen ions (see Section 3.3). Thus, the question of the nature of the magnetic order in $FeBO_3$ at pressures above 50 GPa is currently open and needs further investigation.

A sharp decrease in the insulator gap in $FeBO_3$ predicted and discovered in [71] was subsequently confirmed by RIXS measurements (Fig. 8).

The reason for the decrease in the insulator gap at the SCO in $FeBO_3$ is the sharp decrease in the effective Hubbard parameter U_{eff} at the crossover, from 4.2 eV at $P < P_S$ to 1.45 eV at $P > P_S$ [71]. With a further increase in pressure, the authors of [21] predicted a transition to the state of a nonmagnetic Kondo lattice, in which the band of Hubbard fermions crosses the top of the valence band formed mainly by oxygen p electrons. Such a transition, accompanied by a semiconductor–metal transition, was observed experimentally at a pressure of 163 GPa in [134].

To conclude this section, we return to the question of the effect exerted by cooperativity on the SCO. As noted in the introduction, in the framework of the simplest single-ion model of many-electron terms in a crystal field, the SCO is not a thermodynamic phase transition. Experimental studies of the SCO in 3d metal oxides typically show first-order phase transitions with a jump in volume [5]. In Section 3.3, in the framework of the simplified two-band Hubbard–Kanamori model, we considered the cooperative effects due to the effective interatomic exchange interaction. A more realistic SCO model corresponding to the situation in $FeBO_3$ was considered in [135]. In addition to the HS terms with $S = 5/2$ and LS terms $S = 1/2$, interatomic exchange interactions J_{HS} of the AFM type and J_{LS} of the FM type were taken into account in accordance with [66]. In addition, the second mechanism of cooperativity between cations via coupling to lattice vibrations was also taken into account. Due to the large (about 10%) difference in the ion radii, the SCO leads to a noticeable local deformation of the MeO_6 octahedron,

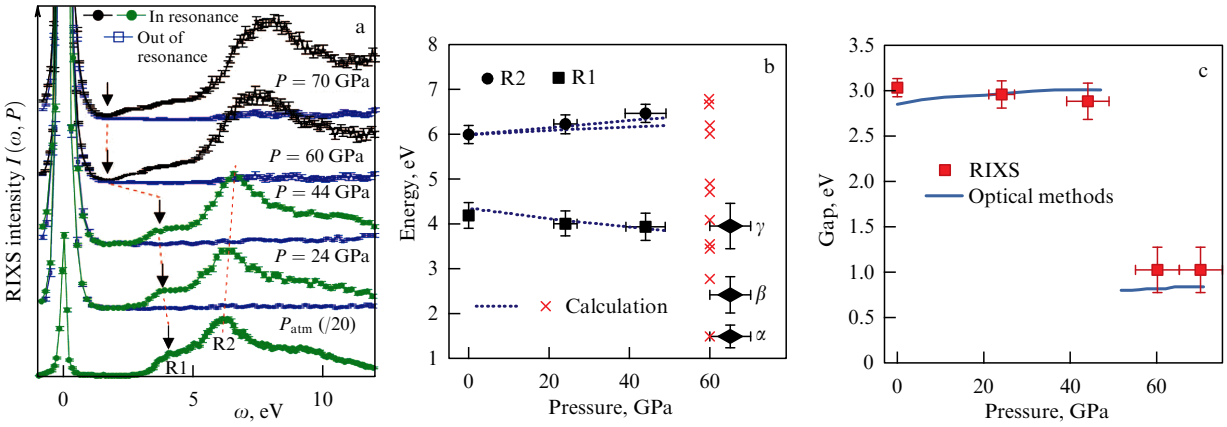

Figure 8. (a) Changes in the RIXS spectra of $FeBO_3$ under SCO, directly showing a decrease in the insulator gap (arrows); spectrum at atmospheric pressure P_{atm} is reduced by a factor of 20. (b) Mott–Hubbard excitation energies calculated from spectra presented in Fig. a. (c) Comparison of the insulator gap values according to RIXS data and optical absorption spectra. (Adapted from [22].)

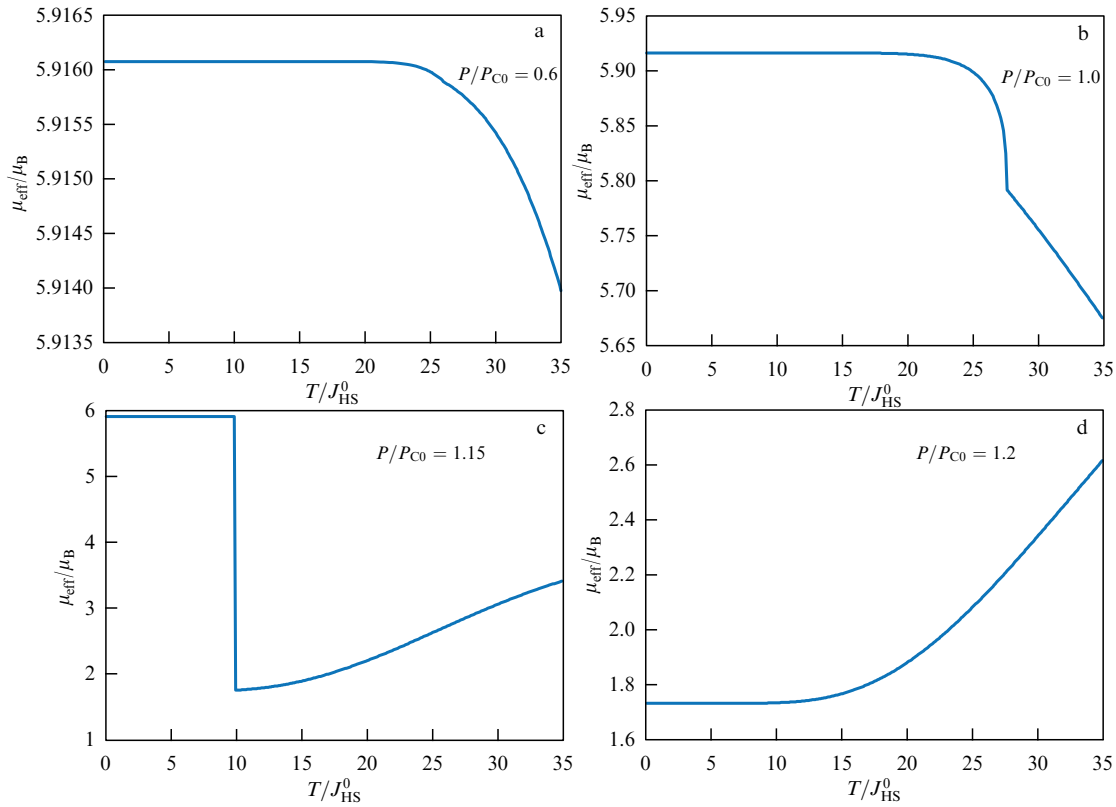

Figure 9. Dependence of the effective magnetic moment on temperature at different pressures: (a) $P/P_{C0} = 0.6$, (b) $P/P_{C0} = 1.0$, (c) $P/P_{C0} = 1.15$, and (d) $P/P_{C0} = 1.2$ [135].

which cause the strong interaction of electrons with local vibrons in the MeO_6 octahedron. Cooperativity in organometallic complexes due to the interaction of neighboring cation–anion groups via an elastic system is usually described in terms of the effective Ising model [136]. The cooperativity effect also manifests itself in the form of temperature-dependent characteristics of the system and in thermodynamic phase transitions [12–15]. In the mean-field approximation with two AFM sublattices in the HS state and an FM LS state, and with the lattice order parameter q characterizing the local deformation of the cation–anion octahedron, phase diagrams are calculated on the pressure–temperature plane with the SCO in the form of a first-order phase transition with the jump in the magnetization, concentration of HS states, and volume described by q [135]. It is interesting to follow the change in the effective magnetic moment $\mu_{eff}(P,T) = \mu_B g[nS_1(S_1+1) + (1-n)S_2(S_2+1)]^{1/2}$ with temperature at different pressures (Fig. 9).

At pressures below the SCO (Fig. 9a, b), the magnetic moment has the maximum value $\mu_{eff}^{HS} = \mu_B g\sqrt{S_1(S_1+1)} = 5.92\mu_B$ at low temperatures, but decreases due to the admixture of LS states at high temperatures. In Fig. 9c, near the crossover at low temperatures, the leading contribution is made by the HS term, but the subsequent sharp decrease in the magnetic moment is associated with the crossover, and a further gradual increase, as in Fig. 9d, with the thermal admixture of HS states to the LS term with the magnetic moment $\mu_{eff}^{LS} = \mu_B g\sqrt{S_2(S_2+1)} = 1.73\mu_B$.

5. Effect of multiplicity fluctuations on the electronic, transport, magnetic, thermodynamic, and optical properties of rare-earth cobaltites $R\mathrm{CoO_3}$

$LaCoO_3$ is a basic representative of a series of rare-earth cobaltites with the formula $R^{3+}Co^{3+}O_3^{2-}$. The transitional and rare-earth elements have the same valency, equal to three. According to neutron diffraction data [24], the crystal structure of $LaCoO_3$ is described by the model of a rhombohedrally distorted perovskite (space group $R\bar{3}c$, D_{3d}^6), whose characteristic feature is the isotropy of oxygen octahedra, which have the same lengths of the valence bonds Co–O and the same Co–O–Co bond angles. Thus, in the $LaCoO_3$ compound, the cobalt ion is surrounded by a slightly distorted oxygen octahedron, forming CoO_6 complexes. In stoichiometric compounds, there is only one type of position for the transition-element ion.

In an isolated CoO_6 octahedron, under the action of the crystal field, the fivefold-degenerate d level splits into two levels belonging to the group of states $t_{2g}(d_{xy}, d_{yz}, d_{zx})$ and $e_g(d_{x^2-y^2}, d_{3z^2-r^2})$. In the 3d shell of the ion, there are six electrons for Co^{3+}, which can form the HS ($S = 2$), LS ($S = 0$), and intermediate-spin (IS, $S = 1$) terms. The $10Dq$ crystal field is so strong that the ground-state term is an LS singlet, while the HS and IS terms are low-energy excitations [137]. As a result, already at temperatures starting from 100 K, and even more so at room temperature and above, the population of magnetic terms is significant, giving rise to complex and unusual electrical, magnetic, and structural properties of $LaCoO_3$ and other rare-earth cobaltites. The study of the scattering of polarized neutrons [138] and the Knight shift in [139] directly confirmed that cobalt ions are in an LS state at low temperatures, while paramagnetic properties appear at temperatures above 100 K. A review of the unusual properties of $LaCoO_3$ and other rare-earth oxides can be found in [6]. In what follows, we mainly discuss new experimental data and their analysis in the framework of the LDA + GTB approach described above. There are several studies in the literature [81, 140] investigating the unusual properties of $LaCoO_3$ in the framework of the two-orbital Hubbard model of the type described in Section 3.4. In the DMFT approximation, the authors of the above papers study the effect of an external field on systems that are close to instability due to the formation of exciton condensates and ordered spin states. Within the same model, it was shown that thin $LaCoO_3$ films on tensile substrates can be ordered ferromagnetically [141]. This was demonstrated experimentally in [142, 143].

5.1 Strong temperature dependence of the electron structure and magnetic and thermodynamic properties of cobaltites

The most appropriate method to describe the electron structure of $LaCoO_3$ with electron correlations and the presence of several multielectron terms manifestly taken into account is LDA + GTB. To find most of the parameters of Hamiltonian (1) from first principles, a standard LDA calculation was done first, after which the Wannier functions were calculated and the parameters of the tight-binding Hamiltonian for the multiband p–d model were found [46]. The validity of the found parameters is corroborated by the complete coincidence of the dispersion of all p–d bands calculated in the LDA and in the tight-binding method.

The many-electron terms of the electrically neutral configuration with six electrons, the hole configuration with five electrons, and the electron configuration with seven electrons were obtained in [144] from calculations in the framework of the crystal field theory, taking the spin–orbit coupling and the covalent admixture of oxygen orbitals into account. Figure 10 shows not only the terms of these three configurations but also Fermi quasiparticles (electron excitations from d^6 to d^7 and hole excitations from d^6 to d^5). Because the spectral weight of a Hubbard fermion is determined by the sum of the occupation numbers of the initial and final states, as can be seen from the numerator of the Green's function (8), the band structure of Hubbard fermions depends on temperature. At $T = 0$, only the LS ground-state term d^6 is filled. Fermi-type excitations have spin 1/2, and hence nonzero matrix elements are only possible for excitations to the final LS state d^7 with $S = 1/2$ (solid arrow). These electron-type excitations form the bottom of the quasiparticle conduction band. Two hole excitations, also shown by solid arrows in Fig. 10, into the final LS states d^5 with $S = 1/2$ form the top of the valence band at $T = 0$. Their band structure is shown in Fig. 11a.

As the temperature increases, the lower sublevels of the HS d^6 term with $J = 1$ and $J = 2$ are populated and new Hubbard fermions with a nonzero spectral weight appear, including hole excitations between the d^6 and d^5 HS terms, shown with dashed lines in Fig. 10. Their spectral weight increases as n_{HS} as the temperature increases. The position of these thermally induced states is seen in Fig. 11.

The appearance of thermally induced in-gap states sharply reduces the width of the insulator gap in Fig. 11b; at $T = 600$ K, the gap disappears and a metallic state appears. The temperature dependence of the band gap calculated in [46] qualitatively reproduces the experimental temperature dependence of the resistance (Fig. 12a). The average value of the squared angular momentum on the Co^{3+} ion also depends on temperature,

$$\langle J^2 \rangle = \sum_p \langle p|J^2|p\rangle \langle X^{p,p}\rangle \,.$$

Here, the sum ranges all occupied levels of the electrically neutral term, and as the population of HS states increases, so does the average angular momentum $J_{\mathrm{av}} = \sqrt{\langle J^2\rangle}$ (Fig. 12b). As can be seen from the figure, the total angular momentum tends to 2 for HS at $T > 1000$ K. At $T = 150$ K, the susceptibility shows a maximum and its consistency with the Curie law is often attributed to the IS, but this is still the contribution from the partially populated HS state. The IS term lies rather high, more than 0.5 eV higher [109], and is not populated in the considered temperature range. The experimental data on the temperature dependence of the magnetic susceptibility also show a broad peak in the range $T = 600$–700 K. According to the calculations in [46], it is associated with the addition of the Pauli contribution from band electrons during the transition to the metallic state. Thus, an accurate calculation of the electronic and magnetic properties taking electronic correlations into account does not require the introduction of the concept of a two-stage spin transition, LS–IS at $T = 150$ K and IS–HS at $T = 650$ K, which was proposed for describing two maxima in the magnetic susceptibility [147].

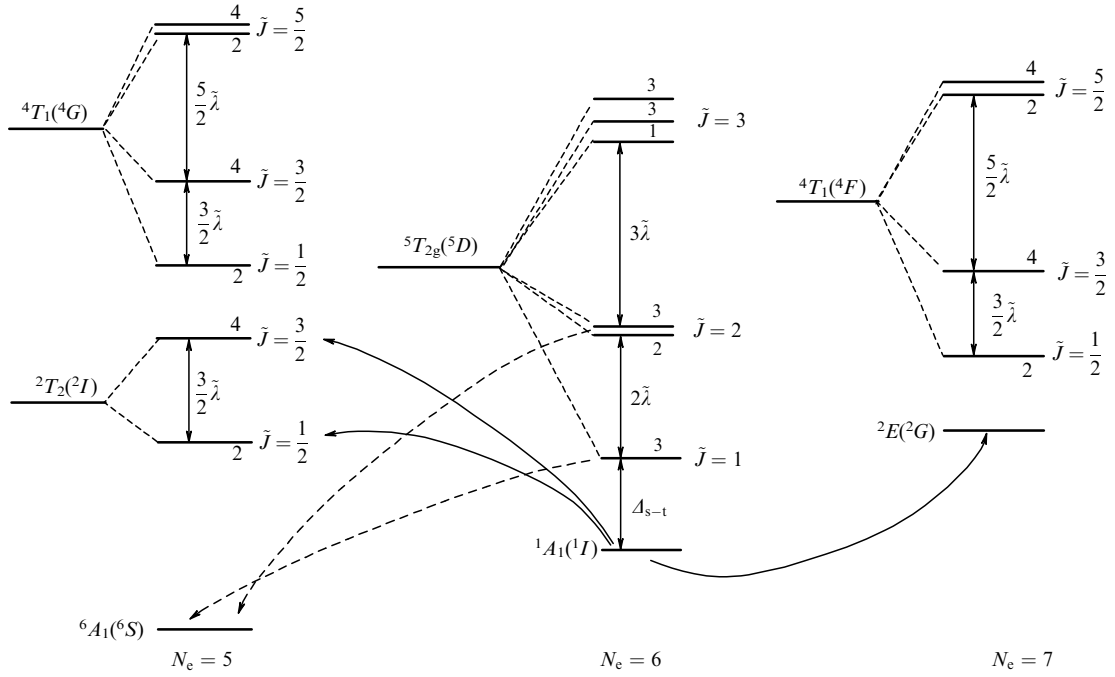

Figure 10. Many-electron terms of electrically neutral configuration with six electrons, a hole configuration with five electrons, and an electron configuration with seven electrons. At $T = 0$, two solid arrows connecting d^6 ground state to d^5 excited states represent Hubbard fermions at the top of the valence band. Arrow from d^6 to d^7 LS state represents fermions at the bottom of the conduction band. At a finite temperature, HS sublevels with total angular momenta $J = 1$ and $J = 2$ are populated; relevant hole excitations are shown with dashed arrows [46].

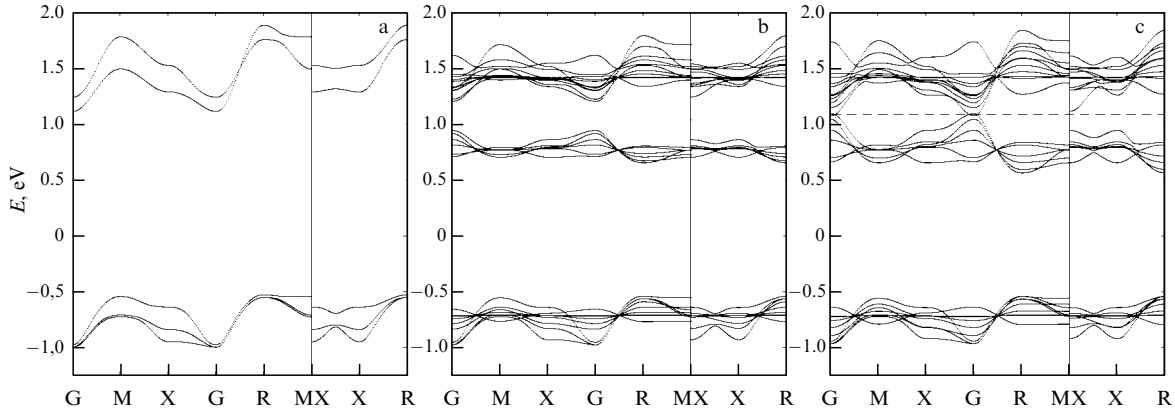

Figure 11. LDA + GTB band structure of $LaCoO_3$ at (a) $T = 0$, (b) $T = 100$ K, and (c) $T = 600$ K [46].

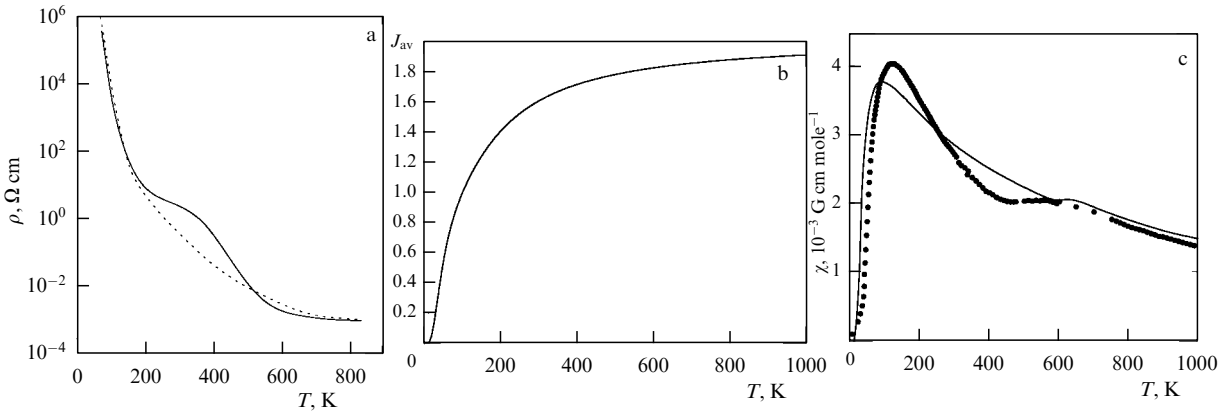

Figure 12. Temperature dependences of (a) resistance, (b) average angular momentum J_{av} on the Co^{3+} ion, and (c) magnetic susceptibility obtained in the LDA + GTB calculation. Solid curve in (a) shows experimental data [145], dotted line shows results of calculations [46]. Solid curve in (c) shows the calculation results; dots show the experimental dependence [146].

5.2 Influence of lanthanide contraction on the spin gap width in the $RCoO_3$ series

When La is replaced with another rare-earth element R, in principle, the same phenomena are observed as in $LaCoO_3$, but the maxima in the temperature dependences of the thermal expansion and magnetic susceptibility anomalies shift toward high temperatures (Fig. 13). Obviously, such a shift is associated with an increase in the spin gap ε_S due to lanthanide contraction. Replacing La with another rare-earth element R results in chemical pressure. Using the Birch–Murnaghan equation of state, with a known value of the spin gap for $LaCoO_3$, we can obtain an estimate of the spin gap for all rare-earth cobaltites (Fig. 14).

Thermal expansion of the lattice leads to an increase in the Co–O bond length and a decrease in the spin gap. The temperature dependence of the spin gap was proposed in [148] in the form

$$\Delta_S(T) = \Delta_0\left[1 - \left(\frac{T}{T_S}\right)^n\right], \tag{28}$$

where Δ_0 is the gap width at $T = 0$ and T_S is the gap closure temperature, which were considered fitting parameters in [148]. For example, for $GdCoO_3$, they were determined as $\Delta_0 = 2260$ K, $T_S = 717$ K, and $n = 3.39$. According to Fig. 14, $\Delta_0 \approx 2000$ K, which qualitatively agrees with the conclusions in [148]. Determining the same parameters from the temperature dependence of the contribution of Co^{3+} to the total paramagnetic susceptibility for $GdCoO_3$ gives similar values $\Delta_0 = 2300$ K, $T_S = 800$ K, and $n = 4$ [150].

To describe the anomalously large thermal expansion in cobaltites, the following approach was proposed in [150]. At each temperature, there is a certain concentration of HS and LS phases. The average volume of a crystal at a given temperature can be written as

$$V(T) = V_{HS}(T)\,n_{HS}(T) + V_{LS}(T)\,n_{LS}(T),$$
$$V_{HS}(T) = V_{HS}(0)(1 + \alpha_{HS}T),$$
$$V_{LS}(T) = V_{LS}(0)(1 + \alpha_{LS}T),$$

where the thermal expansion coefficients α_{HS} and α_{LS} are introduced to describe the lattice anharmonicity.

The temperature dependences $n_{HS}(T)$ and $n_{LS}(T) = 1 - n_{HS}(T)$ are determined by the spin gap (28) as

$$n_{HS} = \frac{g_{HS}\exp\left(-\Delta_S/k_BT\right)}{1 + g_{HS}\exp\left(-\Delta_S/k_BT\right)}, \tag{29}$$

with the degeneration multiplicity of the HS term with $S = 2$ and $L = 1$ given by $g_{HS} = 15$. The zero-temperature volumes were calculated in the DFT framework assuming that $\langle S_z\rangle = 2$ for HS and $\langle S_z\rangle = 0$ for LS. The contribution from multiplicity fluctuations (not including the lattice anharmonicity) can also be taken into account as

$$V_S(T) = V_{HS}(0)\,n_{HS}(T) + V_{LS}(0)\,n_{LS}(T).$$

A comparison of the peaks of the thermal expansion curves with experimental data shows that the leading contribution is made by the interaction of the lattice with multiplicity fluctuations, which determines the anomalously large thermal expansion coefficient $\sim 10^{-4}$. The lattice anharmonicity in the HS state makes a significant contribution at T of the order of 1000 K and above.

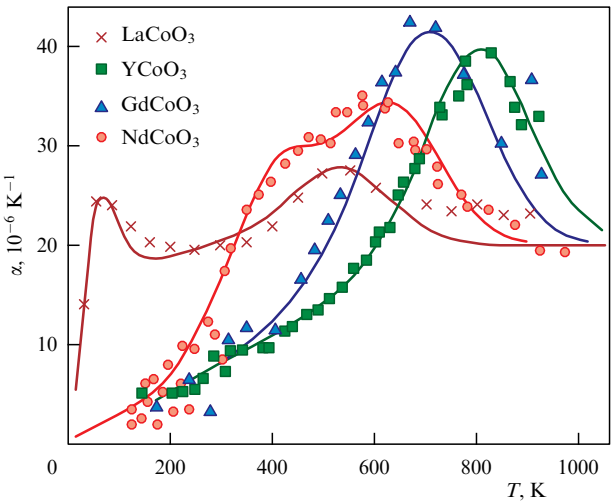

Figure 13. Lattice thermal expansion anomalies in a series of rare-earth cobaltites [148].

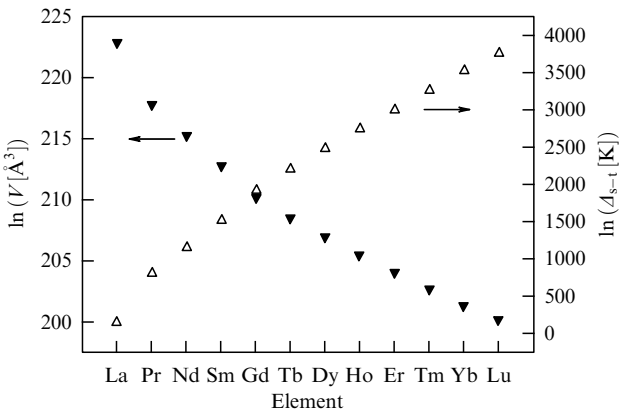

Figure 14. Unit cell volume and spin gap for the entire series of rare-earth cobaltites [149].

5.3 Exchange interaction between excited HS terms of Co^{3+}, exchange sign reversal at spin crossover

We consider the formation of the exchange interaction between excited HS terms of Co^{3+} ions in $LaCoO_3$. A schematic of several lower terms in three sectors of the Hilbert space is shown in Fig. 15: the d^6 neutral sector, the d^5 hole sector, and the d^7 electron sector. Each partial contribution to the exchange interaction is determined by its electron–hole pair, called exchange loops in [65–67].

With $t_\sigma^2 \approx (3t_\pi)^2$, setting $t_\sigma = t$ and $t_\pi = t/3$, we can write the total exchange as [151]

$$J = \frac{1}{2}\left(\frac{t^2}{U + 3J_H} - \frac{t^2/9}{U - J_H}\right) = 4\,\frac{t^2}{9}\,\frac{U - 1.5J_H}{(U + 3J_H)(U - J_H)}. \tag{30}$$

Here, U is the Hubbard parameter and J_H is the Hund intraatomic exchange for d electrons. For $U = 4$ eV, $J_H = 0.8$ eV, and $t = 0.2$ eV, which is a typical set of parameters for iron group oxides, we have the total AFM exchange $J = 2.43$ meV $= 28.2$ K. Previously, when analyzing the electron paramagnetic resonance spectra for $LaCoO_3$ in strong magnetic fields, an exchange between HS terms was introduced phenomenologically, determined from the fitting

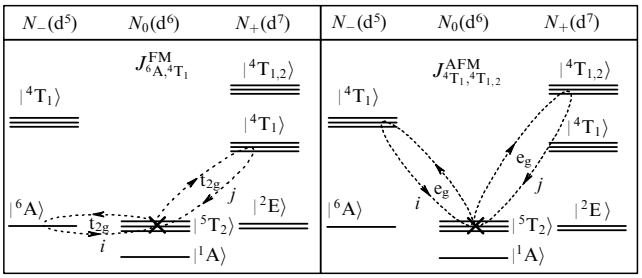

Figure 15. Formation pattern of superexchange interaction between excited HS terms of $LaCoO_3$ (indicated with an $\times$). Exchange loop on the left is formed by the $t_{2g}\pi$ bond and leads to ferromagnetic exchange. Loop on the right is formed due to the e_g bond and makes an AFM contribution [151].

to experimental data, as $J = 29.5$ K [152]. One more comparison with experimental data is possible in terms of the Néel temperature, equal to 200 K for FeO [153]. The Fe^{2+} and Co^{3+} ions share the same sectors of the Hilbert space, and therefore the total exchange between HS terms in them can be compared. With the estimate $J = 28.2$ K obtained in [124] in the framework of the spin-wave theory, $T_N = 226$ K. Thus, for $LaCoO_3$, the AFM contribution exceeds the possible FM contribution.

An analysis of general expression (30) shows that the opposite situation is also possible. Because the condition $U > J_H$ is certainly satisfied, the sign change in (30) is possible due to the numerator. Thus, the AFM wins for $U > 1.5J_H$, while the FM is stronger for $U < 1.5J_H$. Is it possible to reverse the sign of the total exchange by external effects? The Hund exchange is determined by the intraatomic matrix elements, and it can be considered constant. As regards the Hubbard parameter, it is the effective parameter (10). Under SCOs, the Hubbard parameter changes, and not in a universal way. In the transition from HS to LS, U_{eff} decreases for d^5 systems [107], increases for d^3, d^6, and d^8, and does not change for d^2, d^4, and d^7 [106]. Applied to $LaCoO_3$, with Co^{3+} in an LS ground state, possible stabilization of the HS state can lead to a decrease in U_{eff} by $2J_H$. For example, if $U = 3.4J_H$ in the LS state and the total exchange is antiferromagnetic, then $U = 1.4J_H$ after stabilization of the HS state, and the total interaction is ferromagnetic. Possibly, this result explains the appearance of FM ordering, which was observed experimentally on the surface of an $LaCoO_3$ single crystal [154], in grain boundaries [153], and in thin films on tensile substrates [142, 155]. Experimental evidence of the observation of FM and AFM exchanges is presented in [156].

6. Dynamical manifestations of spin crossovers

In Sections 6.1 and 6.2, we discuss two dynamical effects: the sign reversal of the exchange interaction under resonant femtosecond pumping of $FeBO_3$ and the experimental consequences of this effect, as well as theoretical modeling of the possible dynamics of systems with an SCO under a sudden change in the ground state. We note that the study of the dynamics of systems with strong electron correlations under extreme conditions, including at high pressures, is steadily progressing, in particular, with the use of synchrotron methods of infrared and terahertz spectroscopy, whose advances are reflected in review [157].

6.1 Exchange interaction sign reversal under optical pumping of d–d transitions and the ultrafast dynamics in $FeBO_3$

We discuss some aspects of a rapidly developing branch of magnetism, ultrafast magnetism [158–162]. The principal experimental method in this field is the pump–probe technique [163, 164]. Depending on the properties of the magnetic medium, the pump pulse leads to either ultrafast demagnetization or magnetization reversal of the sample, or to the excitation of magnetization precession. As a result of interaction with light, the exchange interaction can vary [165]. Controlling the exchange interaction with subpicosecond pulses is an interesting approach to ultrafast magnetism. The modulation of the exchange interaction by femtosecond laser pulses has been studied experimentally and theoretically [166–182] for various magnetic materials. For the weak ferromagnets $FeBO_3$, Fe_2O_3, and $RFeO_3$, where R is a rare-earth element, the skew angle of two AFM sublattices is determined by the ratio D/J, where D characterizes the Dzyaloshinskii–Moriya interaction and J is the effective interatomic spin exchange of two neighboring Fe^{3+} ions. The excitation of AFM resonance by femtosecond pulses [183] was associated with possible variations in the exchange interaction in the excited state.

The coincidence of the spectral dependences of the amplitude of THz vibrations and the B-absorption band (Fig. 16) indicates the resonant excitation of the $^6A_1 \rightarrow {}^4T_2$ d-transitions in the Fe^{3+} ion from the ground-state term with spin $S = 5/2$ to the excited one with spin $S = 3/2$. In the context of this review, such a change in the population of terms can be called a dynamical SCO. The microscopic mechanism of variation in the exchange interaction between two cations, one excited to the $^4T_2$ state and the other in the $^6A_1$ ground state, is discussed in [64] based on the general approach [65–67].

Under equilibrium conditions, the superexchange interaction is formed by p–d cation–anion–cation electron hops. One spin-up ($\uparrow$) electron hops to the anion with the formation of a virtual pair of $\uparrow\downarrow$ electrons, and then hops backwards, preserving its spin orientation. Another spin-up electron of the anion also virtually hops back and forth to the vacancies in the right-hand cation, all of whose electrons are spin down. Thus, the well-known Kramers–Anderson mechanism is formed. After a photoinduced d–d transition, the spin of one of the electrons of the excited cation is directed strictly opposite to the others, and the total spin of the excited term is 3/2. Virtual hopping of a spin-up electron from the left unexcited cation to oxygen and back occurs in the same way as before the photoexcitation, while, for the right excited cation, the virtual hopping of the second electron from the spin-down oxygen ion and back is possible only when d electrons of the right excited cation and the d electrons of the left cation are directed the same. As a result, both cations are ordered ferromagnetically.

Of course, this is merely an illustration of the many-electron calculation in [64], which demonstrated the AFM exchange between the unperturbed terms and the FM J^{ex}_{ij} for excited Fe^{3+} ions upon pumping d–d transitions into the $A(^4T_1)$ and $B(^4T_2)$ bands of the $FeBO_3$ absorption spectrum. The photoinduced FM contributions to superexchange dominate due to the largest overlap of σ-type oxygen 2p orbitals with d orbitals of the excited $Fe^{3+}(^4T_2)$ ion. At the same time, pumping into the C band does not lead to the formation of photoinduced exchange due to the weak p–d

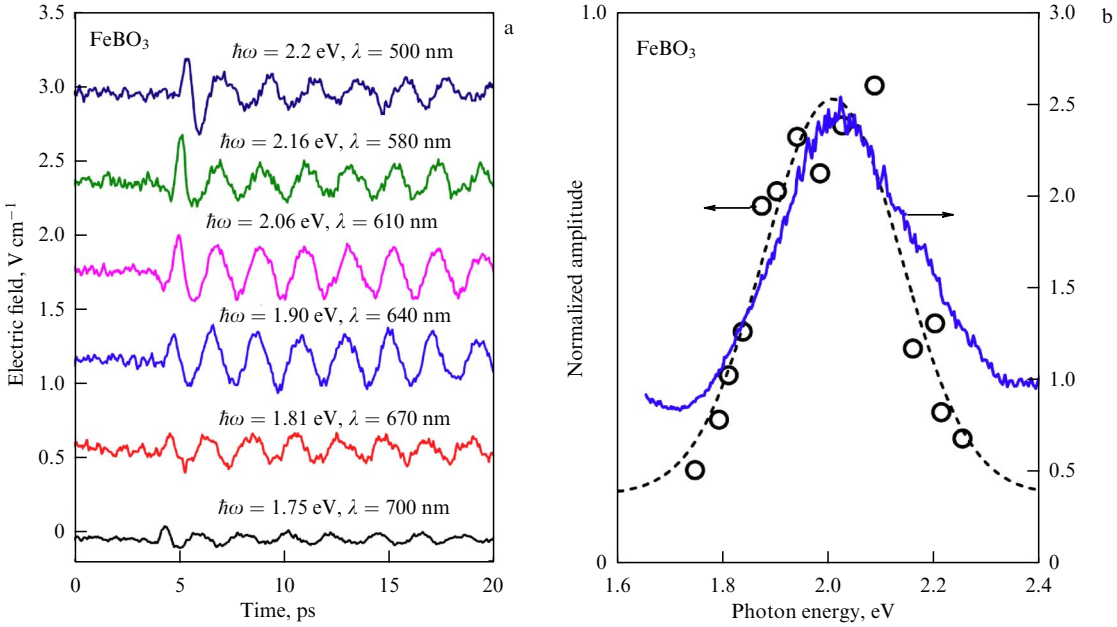

Figure 16. (a) Terahertz oscillations in $FeBO_3$ induced by femtosecond pulses with different wavelengths. (b) Amplitude of THz oscillations and the B-band of the absorption spectrum for the same sample [64].

overlap of orbitals, which is also confirmed in experiment [64].

6.2 Dynamics of spin crossovers under sudden perturbation, change in the dynamics at ultrahigh pressures

In addition to the experiments on the SCO dynamics under optical excitation in organometallic complexes described in the Introduction, data have recently appeared on similar studies in transition-metal oxides. The results of measurements of time-resolved reflection spectra of $LaCoO_3$ single crystals in the soft X-ray range under femtosecond pumping at the BESSY II synchrotron (Berliner Elektronenspeicherring-Gesellschaft für Synchrotronstrahlung MBH II) (Germany) [184] were recently published. This experiment revealed the ultrafast (3 ps) metallization of $LaCoO_3$, attended by a modification of the bond length in CoO_6 octahedra and an increase in the Co–O–Co angle, which is also characteristic of thermal stabilization of HS states.

Below, we consider the ultrafast quantum dynamics of the relaxation of a photoexcited state with a spin different from that of the ground state in magnetically ordered substances, with the electron-vibrational interaction taken into account beyond the adiabatic approximation and with spin–orbit coupling between the HS and LS states. A specific feature of magnetically ordered systems is the presence of interatomic exchange interaction, which, along with elastic interaction, leads to cooperative phenomena near the SCO. The effect of pressure, temperature, and radiation on the SCO has been described using various approaches and approximations [185–195]. In addition to the model consideration of nonadiabatic correlated quantum systems at a finite temperature, there are approaches based on *ab initio* molecular dynamics calculations that use the stochastic Monte Carlo method [196, 197], as well as a description of the dynamics of a photoexcited cis-trans transition beyond the Born–Oppenheimer approximation [198].

For definiteness, we consider the case of d^6 ions (FeO, $(Mg_{1-x}Fe_x)O$, and $LaCoO_3$), with $S_{HS} = S = 2$ and $S_{LS} = 0$. An effective Hamiltonian describing the effect of the exchange interaction on the SCO in such magnetically ordered insulators under pressure, taking the vibronic and spin–orbit couplings into account in the representation of Hubbard X-operators built on HS states with different spin projections $|\sigma\rangle$, $\sigma = -S, -S+1, \ldots +S$, and a singlet LS state $|s\rangle$, can be written as [11]

$$\hat{H}_{\text{eff}} = \hat{H}^{(S)} + \hat{H}^{(e,q)} + \hat{H}_{\text{SO}}\,. \tag{31}$$

Here, the first term on the right-hand side describes the lattice of terms with two spin states, taking the Heisenberg superexchange interaction of HS states into account (see Eqn (17)). The spin gap width $\Delta_S = E_{\text{LS}} - E_{\text{HS}}$ depends linearly on pressure, $\Delta_S = a\,(P_{\text{C0}} - P)$, where P_{C0} is the value of the critical pressure at which $\Delta_S = 0$ and where the crossover would have occurred in the absence of cooperative effects. The linear dependence of the exchange integral J on pressure is also taken into account: $J(P) = J_0 + bP$ [199]. The second term on the right-hand side of (31) contains the energy of totally symmetric intramolecular vibrations, the electron–vibrational (vibronic) interaction [200, 201], and the elastic interaction of 3d metal cations at neighboring sites of the crystal lattice and describes the change in the volume of the system with changes in temperature and external pressure,

$$\hat{H}^{(e,q)} = \sum_i \left(\frac{1}{2}\,k\hat{q}_i^2 + \frac{\hat{p}_i^2}{2M}\right) - \sum_i \left(g_1\hat{q}_i + g_2\hat{q}_i^2\right) \times \left(-X_i^{s,s} + \sum_{\sigma=-S}^{+S} X_i^{\sigma,\sigma}\right) - \frac{1}{2}\,V_q \sum_{\langle i,j\rangle} \hat{q}_i\hat{q}_j\,, \tag{32}$$

where g_1 and g_2 are the intramolecular electron–vibrational coupling constants, k is the elastic coupling constant, $\hat{q}_i$ is the normal coordinate operator corresponding to the breathing regime of ligand vibrations, $\hat{p}_i$ is its conjugate momentum operator, V_q is the elastic intermolecular coupling constant,

and M is the effective mass of the oscillator. Because the ionic radii of the LS and HS states differ significantly (by about 10%) and the eigenfrequencies of the ligands in the LS and HS states are different, $\omega_{\mathrm{LS(HS)}} = \sqrt{k_{\mathrm{LS(HS)}}/M}$, we must take not only linear but also quadratic terms in $\hat{q}$ into account in the electron–vibrational coupling. The elastic coupling constants in the respective LS and HS states are $k_{\mathrm{LS}} = k + 2g_2$ and $k_{\mathrm{HS}} = k - 2g_2$. The third term,

$$\hat{H}_{\mathrm{SO}} = J_x \sum_i \sum_{\sigma=-S}^{+S} \left(X_i^{s,\sigma} + X_i^{\sigma,s} \right), \tag{33}$$

describes the mixing between the HS and LS states induced by the spin-orbit coupling [202]. For definiteness, the following parameters of the Hamiltonian were considered typical for iron oxides: number of nearest neighbors $z = 6$, $a = 80$ K GPa^{-1}, $P_{\mathrm{C0}} = 55$ GPa, $k = 7.5$ eV Å^{-2}, $\omega = 0.05$ eV, $J_x = 0.01$ eV, $g_1 = 0.8$ eV Å^{-1}, $g_2 = 0.75$ eV Å^{-2}, $J_0 = 28$ K, $b = 0.5$ K GPa^{-1}, and $V_q = 0.2$ eV Å^{-1}. Due to anharmonicity in the electron-phonon coupling, the frequencies of local oscillations in the HS and LS states, $\omega_{\mathrm{HS}} = \sqrt{(k - 2g_2)/M}$ and $\omega_{\mathrm{LS}} = \sqrt{(k + 2g_2)/M}$, are distinct. For the chosen parameters, $\omega_{\mathrm{HS}} = 0.045$ eV and $\omega_{\mathrm{LS}} = 0.055$ eV.

The phase diagram of model (31) in the absence of spin-orbit coupling is very similar to the phase diagram of $FeBO_3$, differing in the HS and LS state spins. There are three interrelated order parameters: the local magnetic moment m in the AFM state, the HS term population n, and the change in the length of the cation–anion bond q. The metal–ligand bond length can be represented as $l = l_0 + q$, where l_0 is the regular component due to the ion–covalent chemical bond, which changes due to the anharmonicity of lattice vibrations. The anomalous contribution q arises due to the vibronic interaction. In the absence of spin–orbit coupling, the equilibrium positions of the ligands corresponding to the potential energy minima are determined in the LS and HS states given by $q^0_{\mathrm{LS}} = -g_1/k_{\mathrm{LS}}$ and $q^0_{\mathrm{HS}} = g_1/k_{\mathrm{HS}}$. For the parameter values chosen above, $q^0_{\mathrm{LS}} = -0.09$ Å, $q^0_{\mathrm{HS}} = 0.13$ Å, and $\Delta q^0 = q^0_{\mathrm{HS}} - q^0_{\mathrm{LS}} = 0.22$ Å. Because the bond length l_0 is about 2 Å at $T = 0$, Δq^0 amounts to 10% of this value, which agrees with the known difference between the ionic radii in the LS and HS states. It can be seen that in the absence of electron-vibrational coupling, $q^0_{\mathrm{LS(HS)}} = 0$ and a change in the volume of the system with temperature is only possible due to anharmonicity. At a small value of the spin–orbit coupling $J_x = 0.01$ eV, the shape of the phase diagram is practically unchanged, even though, from the fundamental standpoint, the pressure transition at $T = 0$ is blurred.

When all couplings in (31) are exactly taken into account inside MeO_6 cells in the mean-field approximation for the interatomic exchange and elastic interactions, the wave eigenfunctions can be represented as [203]

$$|\varphi_k\rangle = \sum_{n_{\mathrm{ph}}=0}^{N_{\mathrm{ph}}} \left[a_{n_{\mathrm{ph}},k} |2, 0, n_{\mathrm{ph}}\rangle + \sum_{s_z=-S}^{+S} b_{n_{\mathrm{ph}},s_z,k} |1, s_z, n_{\mathrm{ph}}\rangle \right], \tag{34}$$

where $|\alpha, s_z, n_{\mathrm{ph}}\rangle = |\alpha, s_z\rangle |n_{\mathrm{ph}}\rangle$ is an orthonormal basis of functions given by the direct product of the eigenstates $|\alpha, s_z\rangle$ of spin projection operators with $s_z = -S, (-S+1), \ldots, +S$ for the HS state ($\alpha = 1$) and $s_z = 0$ for the LS state ($\alpha = 2$), and the harmonic oscillator states $|n_{\mathrm{ph}}\rangle = 1/\sqrt{n_{\mathrm{ph}}!}(a^\dagger)^{n_{\mathrm{ph}}}|0, 0, \ldots, 0\rangle$ with $n_{\mathrm{ph}} = 0, 1, 2, \ldots, N_{\mathrm{ph}}$, where N_{ph} is the number of phonons such that for $n_{\mathrm{ph}} > N_{\mathrm{ph}}$, the energy $E_0(N_{\mathrm{ph}} + 1) \approx E_0(N_{\mathrm{ph}})$ of the ground state $|\varphi_0\rangle$ stops changing (within a computation error of less than 1%). When considering various temperature effects, it is necessary to monitor the invariance of not only the ground-state energy but also the energies E_k of the excited states closest to the ground state $|\varphi_k\rangle$. In other words, N_{ph} determines the number of phonons that must be taken into account for a given value of the electron–vibrational interaction in order to form the phonon cloud of the ground and lowest excited states. In our calculations, $N_{\mathrm{ph}} = 300$–500, depending on the parameter values used and the temperature. Multiphonon contributions to polaron states (34) lead to Franck–Condon resonances upon excitation of such states [204].

The temporal dynamics of the SCO is described in [203, 205]. A sudden perturbation was assumed to take the system from the HS state to the LS state. To describe relaxation, we place our system of spins in a thermostat and take the interaction of spin complexes with the thermostat into account. We write the Hamiltonian of the complete system in the form

$$\hat{H} = \hat{H}_0 + \hat{H}_{\mathrm{R}} + \hat{V}, \tag{35}$$

where $\hat{H}_0 = \sum_k E_k |\varphi_k\rangle\langle\varphi_k|$ is Hamiltonian (31) in polaron representation (34), $\hat{V} = \hat{V}_{\mathrm{v\text{–}ph}} + \hat{V}_{\mathrm{s\text{–}ph}} = \sum_q (g_{\mathrm{v\text{–}ph},q} b_q^\dagger a + g^*_{\mathrm{v\text{–}ph},q} b_q a^\dagger) + \sum_q (g_{\mathrm{s\text{–}ph},q} b_q^\dagger \hat{S}^+ + g^*_{\mathrm{s\text{–}ph},q} b_q \hat{S}^-)$ is the coupling between spin system (31) and the thermostat, where $a^\dagger$ (a) are the creation (annihilation) operators for quanta of local oscillations (vibrons) introduced above, $g_{\mathrm{v-ph}}$ and $g_{\mathrm{s-ph}}$ are the respective vibron–phonon and spin–phonon coupling constants, and $\hat{H}_{\mathrm{R}} = \sum_q \hbar\omega_q b_q^\dagger b_q$ is the thermostat Hamiltonian, where $b_q^\dagger$ (b_q) are the creation (annihilation) operators of the thermostat phonons with a wave vector q. The dynamics of the system are assumed to be Markovian and, in terms of the reduced density matrix $\hat{\rho}_0(t)$, are described by the Generalized Master Equation [206] in the Redfield approximation [207], where the transition probabilities are determined by the matrix elements of the interaction of local vibronic and spin degrees of freedom with thermostat phonons; the calculation details can be found in [203, 205].

In experiments on the dynamical SCO, the spin state is usually switched by irradiating the sample with femtosecond light pulses, as in the experiments on $FeBO_3$ and $LaCoO_3$ described in Section 5. Theoretically, this process is modeled as a sudden perturbation (spin state switching) shown in Fig. 17, which illustrates the results of calculating the quantum dynamics of the relaxation of the magnetization m (red line), the HS state population n (blue line), and the displacement q (black line). The calculations were performed for the threefold orbital degeneracy of the HS state at $T = 100$ K and different pressures $P = 0.1P_{\mathrm{C0}}$, $P = 0.5P_{\mathrm{C0}}$, $P = P_{\mathrm{C0}}$, and $P = 1.5P_{\mathrm{C0}}$. The initial photoexcited state $|\psi_0\rangle$ was chosen as the state obtained from the ground state

$$|\varphi_0\rangle = \sum_{n_{\mathrm{ph}}=0}^{N_{\mathrm{ph}}} \left[a_{n_{\mathrm{ph}},0} |2, 0, n_{\mathrm{ph}}\rangle + \sum_{s_z=-S}^{+S} b_{n_{\mathrm{ph}},s_z,0} |1, s_z, n_{\mathrm{ph}}\rangle \right]$$

by switching the quantum numbers α and s_z. For example, if the ground state is the magnetic HS state, then

$$|\psi_0\rangle = \sum_{n_{\mathrm{ph}}=0}^{N_{\mathrm{ph}}} \left[a_{n_{\mathrm{ph}},0} |2, 0, n_{\mathrm{ph}}\rangle + \sum_{s_z=-S}^{+S} b_{n_{\mathrm{ph}},s_z,0} |2, 0, n_{\mathrm{ph}}\rangle \right],$$

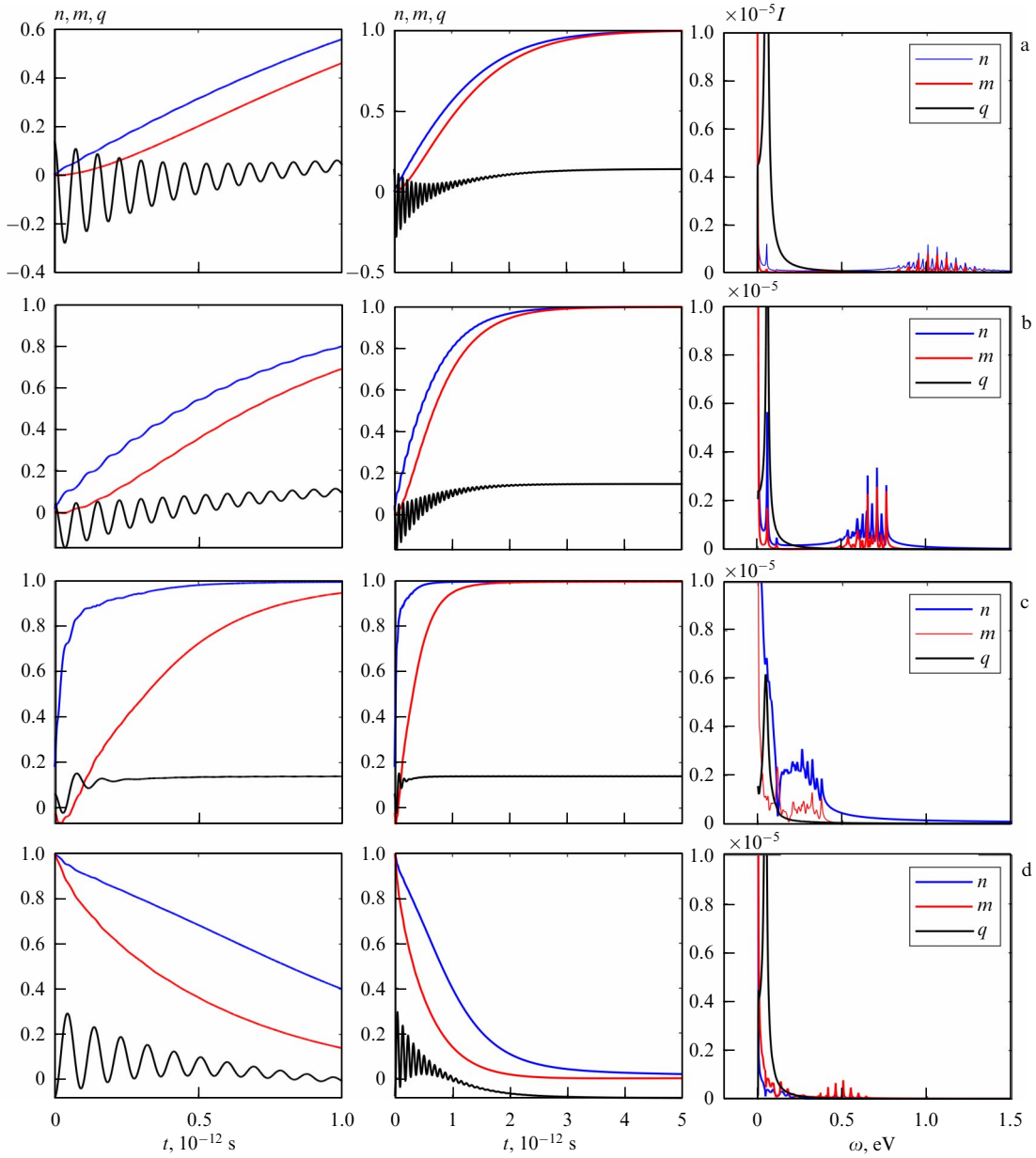

Figure 17. Quantum dynamics of relaxation of photoexcited Franck–Condon states in magnetically ordered substances with SCO at $T = 100$ K and $J_x = 0.01$ eV under pressures (a) $P/P_{C0} = 0.1$, (b) $P/P_{C0} = 0.5$, (c) $P/P_{C0} = 1$, and (d) $P/P_{C0} = 1.5$. Right column shows the results of a Fourier analysis of the time dependences of magnetization m (red line), HS state population n (blue line), and displacement q (black line) used to determined intensity I and frequency ω of spectral components of obtained solutions [203].

while the elastic (phonon) system remained unchanged, i.e., preserved the initial state corresponding to the HS electron configuration of the d ion. Conversely, if the ground state is a nonmagnetic LS state, then

$$|\psi_0\rangle = \sum_{n_{\rm ph}=0}^{N_{\rm ph}} \left[a_{n_{\rm ph},0}|1,+2,n_{\rm ph}\rangle + \sum_{s_z=-S}^{+S} b_{n_{\rm ph},s_z,0}|1,+2,n_{\rm ph}\rangle \right],$$

with the elastic system also preserving the initial state, but now the one corresponding to the LS electron configuration of the d ion. This state switching changes the electron state of the ion, leaving the state of the ligands unchanged. Because the photoexcited state can be decomposed in terms of the basis of eigenstates of the Hamiltonian of an isolated subsystem $|\psi_0\rangle = \sum_k C_{0k}|\varphi_k\rangle$, where $C_{0k} = \langle\varphi_k|\psi_0\rangle$, the initial density matrix has the form $\rho^0_{kk'}(0) = C_{0k}C^*_{0k'}$. At finite temperatures, the subsystem can be in different states with different probabilities, and hence the initial density operator takes the form

$$\hat{\rho}^{\,0}(0) = \frac{1}{Z}\sum_k \exp\left(-\frac{E_k}{k_{\rm B}T}\right)|\psi_k\rangle\langle\psi_k| = \frac{1}{Z}\sum_k\sum_{ii'} \exp\left(-\frac{E_k}{k_{\rm B}T}\right) C_{ik}C^*_{i'k}|\varphi_i\rangle\langle\varphi_{i'}|,$$

where $|\psi_k\rangle = \sum_i C_{ki}|\varphi_i\rangle$ with $C_{ki} = \langle\varphi_i|\psi_k\rangle$, and $k_{\rm B}$ is the Boltzmann constant.

To find the characteristic decay (relaxation) time of photoexcited states, we used the exponential approximation $y_i = y_{0i} + \eta_i \exp(-\xi_i t)$ for the dependence on the magnetization time ($i = m$), the HS state population ($i = n$), and the

displacement ($i = q$), where η_i and ξ_i are fitting parameters, and the equilibrium value y_{0i} was taken from the static self-consistent solution of the mean-field equations. When taken out of equilibrium, the magnetization m, the HS state population n, and the displacement q return to their equilibrium values in different times, with the magnetization having its own relaxation time t_m and the n and q times being practically coincident. This coincidence is unsurprising, because a change in the bond length q is proportional to the ionic radius of the cation. Several time scales of the complex dynamics of the system can be distinguished: the oscillation period of magnetization m, of HS state population n, and of displacement q, as well as the characteristic decay time of the oscillations (the time the system takes to relax to the ground state). We can see a train of perturbations with breaks between them (a wave packet or a train of high-frequency waves with the oscillation energy $\omega_m \sim 1$ eV). Narrow peaks in the Fourier spectrum of a train of high-frequency waves in the right part of Fig. 17 are separated by the frequency interval $\Delta\omega = 58$ meV, which practically coincides with the energy of lattice vibrations $\omega_q = 55$ meV and hence allows identifying the train of high-frequency oscillations with Franck–Condon resonances, which correlate with the minima and maxima of $q(t)$ oscillations. These perturbations decay in the time period τ_q, after which long-lived periodic magnetization oscillations with a period of 140 fs and an energy of 35 meV are observed at low pressures $P/P_{C0} = 0.1$.

Similar low-frequency oscillations of the magnetization during femtosecond pumping of a skewed antiferromagnet $FeBO_3$ at normal pressure were found experimentally in [64, 183] and discussed in Section 5. In these studies, the initial HS state ($S = 5/2$) of the Fe^{3+} ion was excited and transformed into the IS state Fe^{3+} with spin $S = 3/2$, and approximately 4 ps after the excitation, periodic oscillations of the magnetization with a period of about 2 ps were observed. In the calculations in [203, 205], periodic oscillations of the magnetization were established after the return of the electron and elastic systems to the equilibrium HS values in a time of about 2 ps and had a period of 0.14 ps. There is no point in claiming quantitative agreement with experiment, because the parameters of model (31) were not selected specifically for $FeBO_3$. At the same time, the qualitative picture of the oscillations observed in [64, 183] is in reasonable agreement with the theory described here.

7. Spin crossover and metal–insulator transition in ferropericlase. Metal belt inside Earth's lower mantle

In Earth's lower mantle at depths from 600 to 2900 km, pressure and temperature increase with depth from 24 GPa and 2070 K to 135 GPa and 2750 K [208–211]. The Mg-perovskite $Mg_{0.9}Fe_{0.1}SiO_3$ with a low iron content is the predominant mineral (79%) in the lower mantle, the second most dominant, at 16%, being ferropericlase $(Mg_{1-x}Fe_x)O$ with $x = 0.15$–0.25, and the third, $CaSiO_3$ (5%). Therefore, studying their behavior at such pressures and temperatures is very important for understanding the properties of the lower mantle. Perovskite $(Mg,Fe)SiO_3$ can change its structure and shows activation conductivity at all pressures, increasing at pressures of 130–143 GPa [212]. Solid solutions $(Mg_{1-x}Fe_x)O$, called ferropericlase for $x < 0.5$ and magnesiowustite for $x > 0.5$, have more diverse properties and can have a long-range AFM order at an iron concentration exceeding the percolation threshold. Because SCO is possible for FeO, it also takes place in solid solutions. The importance of the SCO for the formation of the lower mantle properties was already noted in [85]. An SCO between the HS ($S = 2$) and LS ($S = 0$) states has been observed in Mössbauer experiments in high-pressure chambers with diamond anvils [213–215]. Subsequent synchrotron measurements of X-ray diffraction of the Mössbauer spectra of $(Mg_{0.75}Fe_{0.25})O$ under hydrostatic conditions [216] established that SCO occurs at room temperature in the pressure range of 55–70 GPa.

The smearing of the SCO observed in high-pressure experiments deserves a separate discussion. If there were no cooperativity effects and the SCO occurred in accordance with the single-ion term picture in the crystal field, then the HS concentration would be given by (29). Then, only at zero temperature would the SCO be accompanied by a sharp change in the concentrations of the HS and LS states, and it would be a quantum phase transition with a Berry-phase-type topological order parameter [10]. But the experimental and theoretical phase diagrams show a sharp first-order phase transition. The reason for the appearance of a sharp transition is related, as discussed in Section 4.2, to cooperative effects. In $FeBO_3$, the Néel temperature in the HS state is above room temperature at all pressures, but in $(Mg_{1-x}Fe_x)O$ it is below room temperature at all pressures [199], and hence measurements with $(Mg_{1-x}Fe_x)O$ at room temperature occur in the para phase under destroyed cooperativity, which forms a diffuse SCO, in accordance with formula (29). A unique experiment to measure the spin states of magnesiowustite at low temperatures and high pressures, for which special chambers with diamond anvils made of nonmagnetic steel have been designed, indeed shows a narrowing of the SCO with decreasing temperature (Fig. 18) [217]. Experimental data in Fig. 18 are in good agreement with subsequent results of LDA + DMFT calculations [218] of the magnetic collapse in $(Mg_{0.75}Fe_{0.25})O$ at megabar pressures. At normal pressure, the calculations give an insulator state with HS states of the Fe^{2+} ion. The crossover region is characterized by the coexistence of Fe^{2+} ions in the HS and LS states, while there are no IS states with $S = 1$. Two types of calculations taking strong correlations into account using the LDA + DMFT [218] and GTB [217] methods gave a similar description of the $(Mg_{0.75}Fe_{0.25})O$ phase diagram.

Under normal conditions, all components of the lower mantle are insulators. At pressures and temperatures typical of the conditions in the lower mantle, some of them can go into the metallic state or change their spin state. We address these questions in what follows. The possibility of the existence of a highly conductive layer in the lower mantle was predicted based on geophysical modeling [219, 220]. Analysis of the data of geophysical MagSat (Magnetic Field Satellite) experiments based on conductivity measurements in the lower mantle led to the conclusion about a jump in conductivity up to 200 S m^{-1} at a depth of 1300 km [221]. Laboratory measurements of the conductivity of Mg perovskite at pressures up to 143 GPa revealed an increase in conductivity after the transition to the post-perovskite phase at pressures above 120 GPa, but without the transition to the metallic state [212]. For ferropericlase, similar measurements in diamond anvil chambers at room temperature revealed a maximum of the pressure dependence of conductivity at a pressure about 60 GPa for the compositions $(Mg_{0.81}Fe_{0.19})O$ [222] and $(Mg_{0.75}Fe_{0.25})O$ [223], associated by the authors with the SCO in the Fe^{2+} ion.

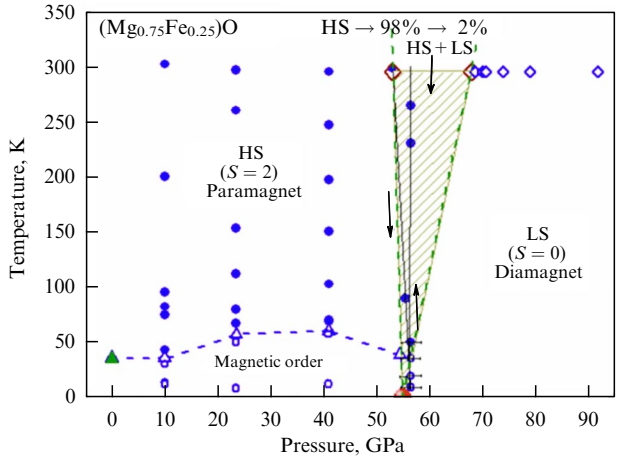

Figure 18. Phase diagram of ferropericlase $(Mg_{0.75}Fe_{0.25})O$ at low temperatures and high pressures. Red dot at $T = 0$ shows the quantum critical point and blue dashed curve at pressures below the SCO shows the Néel temperature as a function of pressure. Shaded triangular region corresponds to a smeared SCO with HS concentrations from 98% to 2%. Dashed straight lines bounding this region, which emerge from the quantum critical point, are plotted in accordance with (29). SCO smearing at $T < 40$ K does not exceed pressure measurement error of the order of 3 GPa [217].

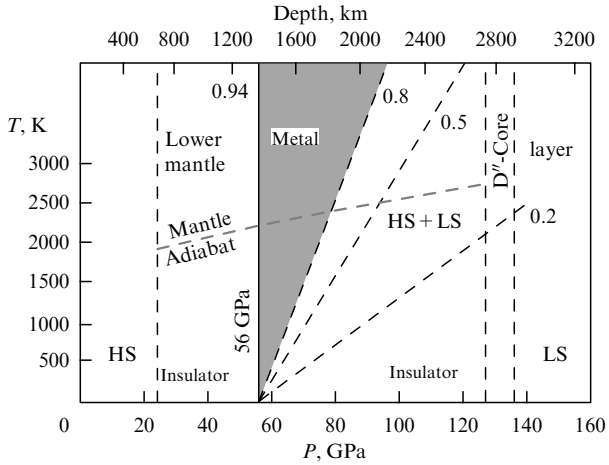

Figure 19. Phase diagram of ferropericlase. Thin vertical dashed lines show the boundaries of Earth's lower mantle, the D″ layer, and the outer core. Terrestrial adiabat (light dashed line) shows the relation between pressure and temperature. Direct rays with a certain concentration of HS states emerge from the quantum critical point at zero temperature. The region of metallic states, outside of which the insulator (semiconductor) region is realized, is shaded [225].

Because ferropericlase is a solid solution of periclase MgO, which is a wide-bandgap insulator, and wustite FeO, which is a classical Mott–Hubbard insulator, theoretical methods invoked to analyze its electron structure must take strong electron correlations into account. In the LDA + GTB framework, such a calculation led to a (P, T) phase diagram with both a metal–insulator transition and an SCO [224]. A comparison of these results with the dependence of pressure and temperature on depth also allows constructing the phase diagram of the ferropericlase states as a function of depth (Fig. 19). At high temperatures, the cooperativity effects are insignificant; because the Néel temperature for ferropericlase is less than 50 K (see Fig. 18), the phase diagram is determined by the condition

$$P = P_C + k_B T \left(2 \frac{\partial (10Dq)}{\partial P} \right)^{-1} \ln \frac{g_{HS}\, n_{LS}}{g_{LS}\, n_{HS}}, \qquad (36)$$

where g_{HS} (g_{LS}) is the degeneration multiplicity of the corresponding terms. For Fe^{2+} in the LS state with $S = 0$ and $L = 0$, $g_{LS} = (2S + 1)(2L + 1) = 1$. In the HS state with $S = 2$ and $L = 1$, $g_{HS} = 15$. If g_{HS} and g_{LS} were equal, the line of maximum fluctuations of $n_{HS} = n_{LS}$ multiplicities would run vertically from the quantum critical point P_C in Fig. 19. Due to the large difference in the degeneracy multiplicities for the Fe^{2+} ion, the $n_{HS} = n_{LS} = 0.5$ line is significantly tilted to the right in Fig. 19. The Mott–Hubbard IMT at a pressure of 60 GPa was theoretically predicted in LDA + DMFT calculations [226]. At low temperatures, the SCO occurs at a pressure of 57 GPa (see Fig. 18). Given the error in determining the pressure (not less than 3 GPa) in diamond anvil experiments, both of these transitions coincide at $T = 0$. As the temperature increases, the IMT line remains vertical in Fig. 19. When moving along the terrestrial adiabat in Fig. 19 deep into Earth, the HS concentration decreases and the LS concentration increases. Because the electron configurations of Fe^{2+} and Co^{3+} coincide, the evolution of the electron structure of ferropericlase as the depth increases is similar to the evolution of the electron structure of $LaCoO_3$ with an increase in the fraction of LS states, i.e., as the temperature decreases. We can see this evolution in Fig. 11: as n_{HS} decreases to 0.8, the metallic state (Fig. 11c) transforms into an insulator state (Fig. 11b). Because such a transition occurs at high temperatures, it cannot be sharp, which is why the transition line from the metal back to the insulator at $n_{HS} = 0.8$ is shown with a dashed line in Fig. 19. At room temperature, the width of the metal region in Fig. 19 is about 10 GPa, which agrees with the measured minimum resistance as a function of pressure in ferropericlase [222].

The phase diagram for ferropericlase (see Fig. 19) was constructed using the results of LDA + DMFT calculations of the FeO electron structure [226]. The metallization of FeO also leads to the metallization of ferropericlase with the iron concentration above the percolation threshold, which is equal to 0.142 for three-dimensional face-centered cubic structures [227]. For the same reason, a mixture of insulating Mg perovskite and metallic ferropericlase is also conductive. In other words, the metallicity of ferropericlase at the concentration that is known for Earth's lower mantle leads to the formation of a metal layer inside Earth at depths determined in Fig. 19 by the intersection of the terrestrial adiabat with the vertical line of the Mott–Hubbard transition and with the line $n_{HS} = 0.8$, which gives the range 1400–1800 km [224, 225] (Fig. 20). An estimate of the conductivity in this layer obtained in [225] is 230 S m^{-1}, which is close to the data in [221], as is the depth at which the conductivity sharply increases: 1400 km in Fig. 19 and 1300 km in [225].

We now consider the effect of SCO in ferropericlase on the elastic properties of the lower mantle. The physical cause of this effect is the difference between the ionic radii of the HS and LS states. Just as multiplicity fluctuations with temperature lead to the thermal expansion anomalies in cobaltites (see Section 5.2), multiplicity fluctuations in the Fe^{2+} ion in ferropericlase cause anomalies in the elastic properties. The thermodynamics of a mixture of spin states with elastic effects taken into account was developed in [228]. The unit cell volumes of ferropericlase in the HS and LS states

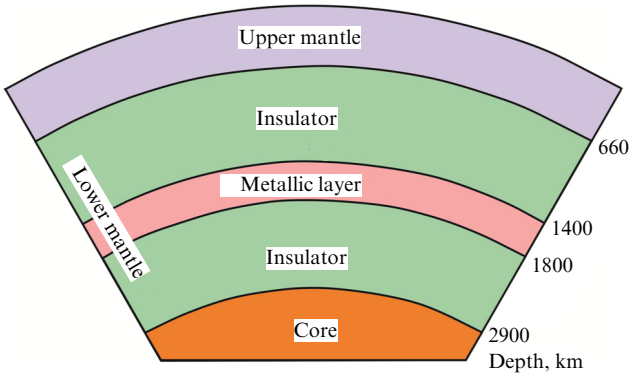

Figure 20. Structure of electrical properties of Earth's lower mantle with a metallic layer at depths of 1400–1800 km [225].

were calculated from the Birch–Murnaghan equation with the parameter $B' = 4$ and the elastic moduli $B_{HS} = 210$ GPa and $B_{LS} = 161$ GPa [229].

The average volume in the mixed state is

$$V(P) = V_{HS}(P)\, n_{HS}(P) + V_{LS}(P)\, n_{LS}(P)\,, \qquad (37)$$

where the HS and LS concentrations are calculated taking the enthalpy $H = E + PV$ into account:

$$n_{HS}(P,T) = \left[1 + \frac{g_{LS}}{g_{HS}} \exp\left(\frac{H_{HS} - H_{LS}}{k_B T}\right)\right]^{-1}. \qquad (38)$$

From Eqn (37), we can determine the elasticity modulus $K^{-1} = -V^{-1}\,\mathrm{d}V/\mathrm{d}P$. The maximum deviation from the linear dependence $K(P)$ is in the center of the region with a depth of 1660–2000 km [230], where anomalies in the propagation velocity of seismic waves were observed [231].

Other manifestations of layer metallization in Earth's lower mantle are associated with the analysis of perturbations of long-term cyclic (11-year), annual, and 27-day geomagnetic variations [232, 233]. The manifestation of electrical conductivity anisotropy in Earth's lower mantle is analyzed in [234], where it is shown that the electrical conductivity tensor elements related to the tangential components of the electromagnetic field can be estimated by analyzing the characteristics of a single magnetic mode. Observational data from a bank of monthly average values of the x, y, and z components of the geomagnetic field for the period from 1920 to 2009 have been processed using the proposed method.

8. Conclusions

The examples of the SCO in the simplest transition-metal oxides discussed above by no means exhaust its possible manifestations. In the literature, one can find examples of SCO in more complex crystals with nonequivalent cations in octahedral and tetrahedral sites, for example, in Co_3BO_5 [235], langasite ($Ba_3TaFe_3Si_2O_{14}$) [236], and ferrite garnet ($Y_3Fe_5O_{12}$) [237]. Extensive literature is devoted to SCO in organometallic complexes, which were not considered in this review. In the coming years, we can expect an increase in the number of studies of dynamical SCO due to the development of new experimental possibilities of terahertz spectroscopy and free-electron lasers.

Acknowledgments. The authors thank the Russian Science Foundation for financial support in the framework of project no. 18-12-00022.

References

1. Cambi L, Szegö L *Ber. dtsch. chem. Ges. A, B* **64** 2591 (1931)
2. Cotton F A, Wilkinson G, Gaus P L *Basic Inorganic Chemistry* 3rd ed. (New York: J. Wiley, 1995)
3. Ksenofontov V, Gaspar A B, Gütlich P, in *Spin Crossover in Transition Metal Compounds III* (Topics in Current Chemistry, Vol. 235, Eds P Gütlich, H A Goodwin) (Berlin: Springer, 2004) p. 23, https://doi.org/10.1007/b95421
4. Gütlich P, Goodwin H A (Eds) *Spin Crossover in Transition Metal Compounds I* (Topics in Current Chemistry, Vol. 233) (Berlin: Springer, 2004) https://doi.org/10.1007/b40394-9
5. Lyubutin I S, Gavriliuk A G *Phys. Usp.* **52** 989 (2009); *Usp. Fiz. Nauk* **179** 1047 (2009)
6. Ivanova N B et al. *Phys. Usp.* **52** 789 (2009); *Usp. Fiz. Nauk* **179** 837 (2009)
7. Tanabe Y, Sugano S *J. Phys. Soc. Jpn.* **9** 766 (1954)
8. Sviridov D T, Smirnov Yu F *Teoriya Opticheskikh Spektrov Ionov Perekhodnykh Metallov* (Theory of Optical Spectra of Transition Metal Ions) (Moscow: Nauka, 1977)
9. Bersuker I B *Elektronnoe Stroenie i Svoistva Koordinatsionnykh Soedinenii. Vvedenie v Teoriyu* (Electronic Structure and Properties of Coordination Compounds. Introduction to Theory) (Leningrad: Khimiya, 1976)
10. Nesterov A I, Ovchinnikov S G *JETP Lett.* **90** 530 (2009); *Pis'ma Zh. Eksp. Teor. Fiz.* **90** 580 (2009)
11. Nesterov A I et al. *Phys. Rev. B* **96** 134103 (2017)
12. Tuchagues J-P et al., in *Spin Crossover in Transition Metal Compounds III* (Topics in Current Chemistry, Vol. 235, Eds P Gütlich, H A Goodwin) (Berlin: Springer, 2004) p. 85, https://doi.org/10.1007/b95423
13. Banerjee H et al. *Phys. Rev. B* **90** 174433 (2014)
14. Boukheddaden K et al. *Magnetochemistry* **2** 17 (2016)
15. Konishi Y et al. *J. Phys. Soc. Jpn.* **75** 114603 (2006)
16. Shatruk M, Avendano C, Dunbar K R, in *Progress in Inorganic Chemistry* Vol. 56 (Ed. K D Karlin) (New York: John Wiley and Sons, 2009) p. 155, https://doi.org/10.1002/9780470440124.ch3
17. Badro J et al. *Phys. Rev. Lett.* **83** 4101 (1999)
18. Lyubutin I S et al. *JETP Lett.* **84** 518 (2006); *Pis'ma Zh. Eksp. Teor. Fiz.* **84** 610 (2006)
19. Ding Y et al. *Phys. Rev. Lett.* **100** 045508 (2008)
20. Troyan I A et al. *JETP Lett.* **74** 24 (2001); *Pis'ma Zh. Eksp. Teor. Fiz.* **74** 26 (2001)
21. Gavriliuk A G et al. *J. Exp. Theor. Phys.* **100** 688 (2005); *Zh. Eksp. Teor. Fiz.* **127** 780 (2005)
22. Kim J et al. *Europhys. Lett.* **108** 37001 (2014)
23. Halcrow M A (Ed.) *Spin-Crossover Materials: Properties and Applications* (Chichester: Wiley, 2013)
24. Cammarata M et al. *Phys. Rev. Lett.* **113** 227402 (2014)
25. Bertoni R et al. *Acc. Chem. Res.* **48** 774 (2015)
26. Duan D et al. *Sci. Rep.* **4** 6968 (2014)
27. Drozdov A P et al. *Nature* **525** 73 (2015)
28. Eremets M I, Drozdov A P *Phys. Usp.* **59** 1154 (2016); *Usp. Fiz. Nauk* **186** 1257 (2016)
29. Izyumov Yu A *Sov. Phys. Usp.* **34** 935 (1991); *Usp. Fiz. Nauk* **161** (11) 1 (1991)
30. Izyumov Yu A *Phys. Usp.* **38** 385 (1995); *Usp. Fiz. Nauk* **165** 403 (1995)
31. Georges A et al. *Rev. Mod. Phys.* **68** 13 (1996)
32. Held K et al. *Int. J. Mod. Phys. B* **15** 2611 (2001)
33. Kotliar G et al. *Rev. Mod. Phys.* **78** 865 (2006)
34. Kuneš J et al. *Eur. Phys. J. Spec. Topics* **180** 5 (2010)
35. Pavarini E et al. (Eds) *The LDA + DMFT Approach to Strongly Correlated Materials. German Research School for Simulation Sciences* (Reihe Modeling and Simulation, Vol. 1) (Jülich: Forschungszentrum. German Research School for Simulation Sciences GmbH, 2011)
36. Izyumov Yu A, Kurmaev E Z *Phys. Usp.* **51** 23 (2008); *Usp. Fiz. Nauk* **178** 25 (2008)

37. Sadovskii M V *Phys. Usp.* **44** 515 (2001); *Usp. Fiz. Nauk* **171** 539 (2001)
38. Rohringer G et al. *Rev. Mod. Phys.* **90** 025003 (2018)
39. Irkhin V Yu, Irkhin Yu P *Electronic Structure, Correlation Effects and Physical Properties of* d- *and* f-*Metals and Their Compounds* (Cambridge: Cambridge Intern. Sc. Publ., 2007); Translated from Russian: *Elektronnaya Struktura, Korrelyatsionnye Effekty i Fizicheskie Svoistva* d- *i* f-*perekhodnykh Metallov i Ikh Soedinenii* 2nd ed., correct. and enlarg. (Moscow–Izhevsk: RKhD, Inst. Komp. Issled., 2008)
40. Ovchinnikov S G, Sandalov I S *Physica C* **161** 607 (1989)
41. Ovchinnikov S G *Phys. Usp.* **40** 993 (1997); *Usp. Fiz. Nauk* **167** 1043 (1997)
42. Korshunov M M et al. *J. Exp. Theor. Phys.* **99** 559 (2004); *Zh. Eksp. Teor. Fiz.* **126** 642 (2004)
43. Korshunov M M et al. *Phys. Rev. B* **72** 165104 (2005)
44. Emery V J *Phys. Rev. Lett.* **58** 2794 (1987)
45. Varma C M et al. *Solid State Commun.* **62** 681 (1987)
46. Ovchinnikov S G et al. *J. Exp. Theor. Phys.* **112** 140 (2011); *Zh. Eksp. Teor. Fiz.* **139** 162 (2011)
47. Schluter M, Hybertsen M S, Christensen N E *Physica C* **153–155** 1217 (1988)
48. McMahan A K, Martin R M, Satpathy S *Phys. Rev. B* **38** 6650 (1988)
49. Zaanen J, Sawatzky G A, Allen J W *Phys. Rev. Lett.* **55** 418 (1985)
50. Lehmann H *Nuovo Cimento* **11** 342 (1954)
51. Ovchinnikov S G *Acta Phys. Polon. B* **34** 431 (2003)
52. Gavrichkov V A et al. *J. Exp. Theor. Phys.* **91** 369 (2000); *Zh. Eksp. Teor. Fiz.* **118** 422 (2000)
53. Gavrichkov V A, Ovchinnikov S G, Yakimov L E *J. Exp. Theor. Phys.* **102** 972 (2006); *Zh. Eksp. Teor. Fiz.* **129** 1103 (2006)
54. Fujimori A, Minami F, Sugano S *Phys. Rev. B* **29** 5225 (1984)
55. van der Laan G et al. *Phys. Rev. B* **23** 4369 (1981)
56. Korshunov M M et al. *Mod. Phys. Lett. B* **26** 1230016 (2012)
57. Zaitsev R O *Sov. Phys. JETP* **41** 100 (1975); *Zh. Eksp. Teor. Fiz.* **68** 207 (1975)
58. Ovchinnikov S, Val'kov V *Hubbard Operators in the Theory of Strongly Correlated Electrons* (London: Imperial College Press, 2004) https://doi.org/10.1142/p314
59. Goodenough J B *Magnetism and the Chemical Bond* (New York: Interscience Publ., 1963)
60. Vonsovskii S V *Magnetism* (New York: J. Wiley, 1974); Translatad from Russian: *Magnetizm* (Moscow: Nauka, 1971)
61. Anderson P W *Solid State Phys.* **14** 99 (1963)
62. Bulaevskii L N et al. *Sov. Phys. JETP* **27** 836 (1968); *Zh. Eksp. Teor. Fiz.* **54** 1562 (1968)
63. Chao K A, Spalek J, Oles A M *J. Phys. C* **10** L271 (1977)
64. Mikhaylovskiy R V et al. *Phys. Rev. Lett.* **125** 157201 (2020)
65. Gavrichkov V A, Polukeev S I, Ovchinnikov S G *Phys. Rev. B* **95** 144424 (2017)
66. Gavrichkov V A, Polukeev S I, Ovchinnikov S G *J. Exp. Theor. Phys.* **127** 713 (2018); *Zh. Eksp. Teor. Fiz.* **154** 835 (2018)
67. Gavrichkov V A, Polukeev S I, Ovchinnikov S G *Phys. Rev. B* **101** 094409 (2020)
68. Irkhin V Yu, Irkhin Yu P *Phys. Status Solidi B* **183** 9 (1994)
69. Irkhin V Yu, Katsnel'son M I, Trefilov A V *J. Exp. Theor. Phys.* **78** 936 (1994); *Zh. Eksp. Teor. Fiz.* **105** 1733 (1994)
70. Kanamori J *Prog. Theor. Phys.* **30** 275 (1963)
71. Gavrilyuk A G et al. *J. Exp. Theor. Phys.* **99** 566 (2004); *Zh. Eksp. Teor. Fiz.* **126** 650 (2004)
72. Kuz'min V I et al. *Phys. Rev. B* **100** 144429 (2019)
73. Hubbard J *Proc. R. Soc. Lond. A* **277** 237 (1964)
74. Knox R *Solid State Physics* (New York: Academic Press, 1963)
75. Keldysh L V, Kopaev Yu V *Sov. Phys. Solid State* **6** 2219 (1965); *Fiz. Tverd. Tela* **6** 2791 (1964)
76. Kuneš J *J. Phys. Condens. Matter* **27** 333201 (2015)
77. Werner P, Millis A J *Phys. Rev. Lett.* **99** 126405 (2007)
78. Balents L *Phys. Rev. B* **62** 2346 (2000)
79. Kaneko T, Ohta Y *Phys. Rev. B* **90** 245144 (2014)
80. Nasu J et al. *Phys. Rev. B* **93** 205136 (2016)
81. Kuneš J, Augustinský P *Phys. Rev. B* **89** 115134 (2014)
82. Orlov Yu S et al. *Phys. Rev. B* **104** 195103 (2021)
83. Mott N F *Metal-Insulator Transitions* 2nd ed. (London: Taylor and Francis, 1990)
84. Austin I G, Mott N F *Science* **168** 71 (1970)
85. Cohen R E, Mazin I I, Isaak D G *Science* **275** 654 (1997)
86. Kuneš J et al. *Nat. Mater.* **7** 198 (2008)
87. Rueff J-P et al. *J. Phys. Condens. Matter* **17** S717 (2005)
88. Yoo C S et al. *Phys. Rev. Lett.* **94** 115502 (2005)
89. Guo Q et al. *J. Phys. Condens. Matter* **14** 11369 (2002)
90. Atou T et al. *Jpn. J. Appl. Phys.* **43** L1281 (2004)
91. Eto T et al. *Phys. Rev. B* **61** 14984 (2000)
92. Potapkin V et al. *Phys. Rev. B* **93** 201110 (2016)
93. Kuneš J et al. *Phys. Rev. Lett.* **102** 146402 (2009)
94. Noguchi Y et al. *Geophys. Res. Lett.* **23** 1469 (1996)
95. Mita Y et al. *Phys. Status Solidi B* **223** 247 (2001)
96. Patterson J R et al. *Phys. Rev. B* **69** 220101 (2004)
97. Yagi T, Suzuki T, Akimoto S *J. Geophys. Res.* **90** 8784 (1985)
98. Fei Y, Mao H-K *Science* **266** 1678 (1994)
99. Pasternak M P et al. *Phys. Rev. Lett.* **79** 5046 (1997)
100. Mattila A et al. *Phys. Rev. Lett.* **98** 196404 (2007)
101. Ohta K et al. *Phys. Rev. B* **82** 174120 (2010)
102. Fang Z et al. *Phys. Rev. B* **59** 762 (1999)
103. Ozawa H et al. *Phys. Rev. B* **84** 134417 (2011)
104. Fischer R A et al. *Geophys. Res. Lett.* **38** L24301 (2011)
105. Ohta K et al. *Phys. Rev. Lett.* **108** 026403 (2012)
106. Ovchinnikov S G *J. Exp. Theor. Phys.* **116** 123 (2013); *Zh. Eksp. Teor. Fiz.* **143** 141 (2013)
107. Ovchinnikov S G *J. Exp. Theor. Phys.* **107** 140 (2008); *Zh. Eksp. Teor. Fiz.* **134** 172 (2008)
108. Gavrichkov V A et al. *JETP Lett.* **112** 241 (2020); *Pis'ma Zh. Eksp. Teor. Fiz.* **112** 258 (2020)
109. Lamonova K V et al. *J. Phys. Chem. A* **115** 13596 (2011)
110. Rechtin M D, Moss S C, Averbach B L *Phys. Rev. Lett.* **24** 1485 (1970)
111. Jiang H et al. *Phys. Rev. B* **82** 045108 (2010)
112. van Elp J et al. *Phys. Rev. B* **44** 1530 (1991)
113. van Elp J et al. *Phys. Rev. B* **44** 6090 (1991)
114. Kurmaev E Z et al. *Phys. Rev. B* **77** 165127 (2008)
115. Pratt G W (Jr.), Coelho R *Phys. Rev.* **116** 281 (1959)
116. Pudalov V M, Gershenson M E *JETP Lett.* **111** 225 (2020); *Pis'ma Zh. Eksp. Teor. Fiz.* **111** 237 (2020)
117. Kuneš J et al. *Phys. Rev. Lett.* **99** 156404 (2007)
118. Kuneš J et al. *Phys. Rev. B* **75** 165115 (2007)
119. Ovchinnikov S G, Ovchinnikova T M *J. Exp. Theor. Phys.* **133** 374 (2021); *Zh. Eksp. Teor. Fiz.* **160** 443 (2021)
120. Stephens D R, Drickamer H G *J. Chem. Phys.* **34** 937 (1961)
121. Reinen D *Ber. Bunsenges. phys. Chem.* **69** 82 (1965)
122. Gavriliuk A G et al. *J. Exp. Theor. Phys.* **92** 696 (2001); *Zh. Eksp. Teor. Fiz.* **119** 799 (2001)
123. Sawatzky G A, Allen J W *Phys. Rev. Lett.* **53** 2339 (1984)
124. Gavriliuk A G, Trojan I A, Struzhkin V V *Phys. Rev. Lett.* **109** 086402 (2012)
125. Massey M J et al. *Phys. Rev. B* **42** 8776 (1990)
126. Anderson P W *Phys. Rev.* **115** 2 (1959)
127. Harrison W A *Elementary Electronic Structure* (Singapore: World Scientific, 1999)
128. Gavriliuk A G et al. *JETP Lett.* **75** 23 (2002); *Pis'ma Zh. Eksp. Teor. Fiz.* **75** 25 (2002)
129. Sarkisyan V A et al. *JETP Lett.* **76** 664 (2002); *Pis'ma Zh. Eksp. Teor. Fiz.* **76** 788 (2002)
130. Ovchinnikov S G *JETP Lett.* **77** 676 (2003); *Pis'ma Zh. Eksp. Teor. Fiz.* **77** 808 (2003)
131. Ovchinnikov S G, Zabluda V N *J. Exp. Theor. Phys.* **98** 135 (2004); *Zh. Eksp. Teor. Fiz.* **125** 150 (2004)
132. Ovchinnikov S G et al. *J. Exp. Theor. Phys.* **131** 177 (2020); *Zh. Eksp. Teor. Fiz.* **158** 184 (2020)
133. Troyan I A et al. *JETP Lett.* **78** 13 (2003); *Pis'ma Zh. Eksp. Teor. Fiz.* **78** 16 (2003)
134. Troyan I A et al. *JETP Lett.* **94** 748 (2011); *Pis'ma Zh. Eksp. Teor. Fiz.* **94** 811 (2011)
135. Orlov Yu S, Nikolaev S V, Ovchinnikov S G *J. Exp. Theor. Phys.* **129** 1062 (2019); *Zh. Eksp. Teor. Fiz.* **156** 1165 (2019)
136. Boukheddaden K et al. *Phase Transit.* **75** 733 (2002)
137. Goodenough J B *J. Phys. Chem. Solids* **6** 287 (1958)

138. Asai K et al. *Phys. Rev. B* **40** 10982 (1989)
139. Itoh M et al. *J. Phys. Soc. Jpn.* **64** 3967 (1995)
140. Sotnikov A, Kuneš J *Sci. Rep.* **6** 30510 (2016)
141. Sotnikov A, Ahn K-H, Kuneš J *SciPost Phys.* **8** 082 (2020)
142. Fuchs D et al. *Phys. Rev. B* **75** 144402 (2007)
143. Liu H et al. *J. Alloys Compd.* **594** 158 (2014)
144. Orlov Yu S, Ovchinnikov S G *J. Exp. Theor. Phys.* **109** 322 (2009); *Zh. Eksp. Teor. Fiz.* **136** 377 (2009)
145. Yamaguchi S et al. *Phys. Rev. B* **53** R2926 (1996)
146. Baier J et al. *Phys. Rev. B* **71** 014443 (2005)
147. Saitoh T et al. *Phys. Rev. B* **55** 4257 (1997)
148. Knížek K et al. *Eur. Phys. J. B* **47** 213 (2005)
149. Ovchinnikov S G, Orlov Yu S, Dudnikov V A *J. Magn. Magn. Mater.* **324** 3584 (2012)
150. Orlov Yu S et al. *Phys. Rev. B* **88** 235105 (2013)
151. Orlov Yu S et al. *Comput. Mater. Sci.* **204** 111134 (2022)
152. Hoch M J R et al. *Phys. Rev. B* **79** 214421 (2009)
153. Fujii A et al. *Am. Mineralogist* **96** 329 (2011)
154. Yan J-Q, Zhou J-S, Goodenough J B *Phys. Rev. B* **70** 014402 (2004)
155. Harada A et al. *Phys. Rev. B* **75** 184426 (2007)
156. Androulakis J, Katsarakis N, Giapintzakis J *Phys. Rev. B* **64** 174401 (2001)
157. Kimura S, Okamura H *J. Phys. Soc. Jpn.* **82** 021004 (2013)
158. Kalashnikova A M, Kimel A V, Pisarev R V *Phys. Usp.* **58** 969 (2015); *Usp. Fiz. Nauk* **185** 1064 (2015)
159. Pyatakov A P et al. *Phys. Usp.* **58** 981 (2015); *Usp. Fiz. Nauk* **185** 1077 (2015)
160. Mukhin A A et al. *Phys. Usp.* **58** 993 (2015); *Usp. Fiz. Nauk* **185** 1089 (2015)
161. Nikitov S A et al. *Phys. Usp.* **58** 1002 (2015); *Usp. Fiz. Nauk* **185** 1099 (2015)
162. Bossini D et al. *ACS Photon.* **3** 1385 (2016)
163. Kimel A V et al. *Nature* **435** 655 (2005)
164. Satoh T et al. *Nat. Photon.* **6** 662 (2012)
165. Demokritov S O, Kreines N M, Kudinov V I *JETP Lett.* **41** 46 (1985); *Pis'ma Zh. Eksp. Teor. Fiz.* **41** 38 (1985)
166. Rhie H-S, Durr H A, Eberhardt W *Phys. Rev. Lett.* **90** 247201 (2003)
167. Melnikov A et al. *Phys. Rev. Lett.* **91** 227403 (2003)
168. Wang J et al. *Phys. Rev. Lett.* **98** 217401 (2007)
169. Wall S et al. *Phys. Rev. Lett.* **103** 097402 (2009)
170. Först M et al. *Phys. Rev. B* **84** 241104 (2011)
171. Carley R et al. *Phys. Rev. Lett.* **109** 057401 (2012)
172. Li T et al. *Nature* **496** 69 (2013)
173. Subkhangulov R R et al. *Sci. Rep.* **4** 4368 (2014)
174. Mentink J H, Eckstein M *Phys. Rev. Lett.* **113** 057201 (2014)
175. Matsubara M et al. *Nat. Commun.* **76** 6724 (2015)
176. Mentink J H, Balzer K, Eckstein M *Nat. Commun.* **6** 6708 (2015)
177. Frietsch B et al. *Nat. Commun.* **6** 8262 (2015)
178. Johansson J O et al. *Chem. Sci.* **7** 7061 (2016)
179. Eich S et al. *Sci. Adv.* **3** e1602094 (2017)
180. Tengdin Ph et al. *Sci. Adv.* **4** eaap9744 (2018)
181. Maehrlein S F et al. *Sci. Adv.* **4** eaar5164 (2018)
182. Afanasiev D et al. *Phys. Rev. X* **9** 021020 (2019)
183. Mikhaylovskiy R V et al. *Nat. Commun.* **6** 8190 (2015)
184. Izquierdo M et al. *Commun. Phys.* **2** 8 (2019)
185. Kambara T *J. Phys. Soc. Jpn.* **49** 1806 (1980)
186. Sasaki N, Kambara T *J. Chem. Phys.* **74** 3472 (1981)
187. Sasaki N, Kambara T *Phys. Rev. B* **40** 2442 (1989)
188. Koshino K, Ogawa T *J. Phys. Soc. Jpn.* **68** 2164 (1999)
189. Biernacki S W, Clerjaud B *Phys. Rev. B* **72** 024406 (2005)
190. Chang J, Fedro A J, van Veenendaal M *Phys. Rev. B* **82** 075124 (2010)
191. van Veenendaal M, Chang J, Fedro A J *Phys. Rev. Lett.* **104** 067401 (2010)
192. Klokishner S, Linares J *J. Phys. Chem. C* **111** 10644 (2007)
193. Klinduhov N, Chernyshov D, Boukheddaden K *Phys. Rev. B* **81** 094408 (2010)
194. Boukheddaden K, Nishino M, Miyashita S *Phys. Rev. Lett.* **100** 177206 (2008)
195. D'Avino G, Painelli A, Boukheddaden K *Phys. Rev. B* **84** 104119 (2011)
196. Mazzola G, Zen A, Sorella S *J. Chem. Phys.* **137** 134112 (2012)
197. Tubman N M et al. *Phys. Rev. A* **90** 042507 (2014)
198. Levine B G, Martínez T J *Annu. Rev. Phys. Chem.* **58** 613 (2007)
199. Lyubutin I S, Ovchinnikov S G *J. Magn. Magn. Mater.* **324** 3538 (2012)
200. Lipari N O, Duke C B, Pietronero L *J. Chem. Phys.* **65** 1165 (1976)
201. Painelli A, Girlando A *J. Chem. Phys.* **84** 5655 (1986)
202. Griffith J S *The Theory of Transition-Metal Ions* (Cambridge: Cambridge Univ. Press, 1961)
203. Orlov Yu S et al. *JETP Lett.* **112** 250 (2020); *Pis'ma Zh. Eksp. Teor. Fiz.* **112** 268 (2020)
204. Sawatzky G A *Nature* **342** 480 (1989)
205. Orlov Yu S et al. *J. Exp. Theor. Phys.* **132** 399 (2021); *Zh. Eksp. Teor. Fiz.* **159** 479 (2021)
206. Blum K *Density Matrix Theory and Applications* 3rd ed. (Springer Series on Atomic, Optical, and Plasma Physics, Vol. 64) (Heidelberg: Springer, 2012)
207. Redfield A G *Adv. Magn. Opt. Res.* **1** 1 (1965)
208. Dobretsov N I, Kirdyashkin A G, Kirdyashkin A A *Glubinnaya Geodinamika* (Deep Geodynamics) (Novosibirsk: Izd. SO RAN, Filial GEO, 2001)
209. Stacey F D, Davis P M *Physics of the Earth* 4th ed. (Cambridge: Cambridge Univ. Press, 2008)
210. Pushcharovskii Yu M, Pushcharovskii D Yu *Geologiya Mantii Zemli* (Geology of the Earth's Mantle) (Moscow: GEOS, 2010)
211. Xu Y, Shankland T J, Poe B T *J. Geophys. Res.* **105** 27865 (2000)
212. Ohta K et al. *Science* **320** 89 (2008)
213. Badro J et al. *Science* **300** 789 (2003)
214. Gavriliuk A G et al. *JETP Lett.* **84** 161 (2006); *Pis'ma Zh. Eksp. Teor. Fiz.* **84** 190 (2006)
215. Kantor I Yu, Dubrovinsky L S, McCammon C A, in *Proc. of the Joint 20th AIPART — 43rd EHPRG, Intern. Conf. on High Pressure Science and Technology, June 27 – July 1, 2005, Karlsruhe, Germany* (Eds E Dinjus, N Dahmen) (Karlsruhe: Forschungszentrum Karlsruhe, 2005) T5-P101
216. Lyubutin I S et al. *JETP Lett.* **90** 617 (2009); *Pis'ma Zh. Eksp. Teor. Fiz.* **90** 681 (2009)
217. Lyubutin I S et al. *Proc. Natl. Acad. Sci. USA* **110** 7142 (2013)
218. Skorikov N A et al. *J. Phys. Condens. Matter* **27** 275501 (2015)
219. Porokhova L N, Abramova D Yu, Porokhov D A *Earth Planets Space* **51** 1067 (1999)
220. Buffett B A, Garnero E J, Jeanloz R *Science* **290** 1338 (2000)
221. Constable S, Constable C *Geochem. Geophys. Geosyst.* **5** (1) 3 (2004)
222. Ohta K et al. *Proc. Jpn. Acad. B* **83** 97 (2007)
223. Lin J F et al. *Geophys. Res. Lett.* **34** L16305 (2007)
224. Ovchinnikov S G *JETP Lett.* **94** 192 (2011); *Pis'ma Zh. Eksp. Teor. Fiz.* **94** 210 (2011)
225. Ovchinnikov S G et al. *JETP Lett.* **96** 129 (2012); *Pis'ma Zh. Eksp. Teor. Fiz.* **96** 135 (2012)
226. Shorikov A O et al. *Phys. Rev. B* **82** 195101 (2010)
227. Ziman J M *Models of Disorder*: *the Theoretical Physics of Homogeneously Disordered Systems* (Cambridge: Cambridge Univ. Press, 1979)
228. Hsu H et al. *Rev. Mineral. Geochem.* **71** 169 (2010)
229. Lin J-F et al. *Nature* **436** 377 (2005)
230. Ovchinnikov S G et al. *J. Phys. Conf. Ser.* **653** 012095 (2015)
231. Cobden L et al. *J. Geophys. Res.* **114** B11309 (2009)
232. Plotkin V V, Dyad'kov P G, Ovchinnikov S G *Russ. Geol. Geophys.* **54** 263 (2013); *Geol. Geofiz.* **54** 345 (2013)
233. Plotkin V V, Dyad'kov P G, Ovchinnikov S G *Russ. Geol. Geophys.* **55** 1138 (2014); *Geol. Geofiz.* **55** 1436 (2014)
234. Plotkin V V, Dyad'kov P G, Ovchinnikov S G *Russ. Geol. Geophys.* **56** 1772 (2015); *Geol. Geofiz.* **56** 2240 (2015)
235. Kazak N V et al. *Phys. Rev. B* **103** 094445 (2021)
236. Gavriliuk A G et al. *Appl. Phys. Lett.* **103** 162402 (2013)
237. Lyubutin I S et al. *JETP Lett.* **82** 702 (2005); *Pis'ma Zh. Eksp. Teor. Fiz.* **82** 797 (2005)